Mapping Alzheimer's Molecular Pathologies in Large-Scale Connectomics Data: A Publicly Accessible Correlative Microscopy Resource

Xiaomeng Han[1*], Peter H. Li[2], Shuohong Wang[1], Tim Blakely[2], Sneha Aggarwal[3], Bhavika Gopalani[3], Morgan Sanchez[4], Richard Schalek[1], Yaron Meirovitch[1], Zudi Lin[5], Daniel Berger[1], Yuelong Wu[1], Fatima Aly[6], Sylvie Bay [7], Benoît Delatour [8], Pierre Lafaye[9], Hanspeter Pfister[5], Donglai Wei[3], Viren Jain[2], Hidde Ploegh[10], Jeff Lichtman[1*]

[1] Department of Molecular and Cellular Biology, Harvard University, Cambridge, MA

[2] Google Research, Mountain View, CA

[3] Computer Science Department, Boston College, Chestnut Hill, MA

[4] Department of Biomedical Informatics, Harvard Medical School, MA

[5] School of Engineering and Applied Sciences, Harvard University, Cambridge, MA

[6] Harvard College, MA

[7] Institut Pasteur, Université Paris Cité, CNRS UMR 3523, Unité de Chimie des Biomolécules; Paris, France

[8] Paris Brain Institute (ICM), CNRS UMR 7225, INSERM U1127, Sorbonne Université, Hôpital de la Pitié-Salpêtrière; Paris, France

[9] Institut Pasteur, Université Paris Cité, CNRS UMR 3528, Antibody Engineering Platform; Paris, France

[10] Program of Cellular and Molecular Medicine, Boston Children's Hospital, Boston, MA

[*] Corresponding Authors: xiaomenghan@fas.harvard.edu; jeff@mcb.harvard.edu

Abstract

Connectomics using volume-electron-microscopy enables mapping and analysis of neuronal networks, revealing insights into neural circuit function and dysfunction. In Alzheimer's disease (AD), where amyloid-β (Aβ) and hyperphosphorylated-Tau (pTau) are implicated, connectomics offers an approach to unravel how these molecules contribute to circuit alterations by enabling the study of these molecules within the context of the complete local neuronal and glial milieu. We present a volumetric-correlated-light-and-electron microscopy (vCLEM) protocol using fluorescent nanobodies to localize Aβ and pTau within a large-scale connectomics dataset from the hippocampus of the 3xTg AD mouse model. A key outcome of this work is a publicly accessible vCLEM dataset, featuring fluorescent labeling of Aβ and pTau in the ultrastructural context with segmented neurons, glia, and synapses. This dataset provides a unique resource for exploring AD pathology in the context of connectomics and fosters collaborative opportunities in neurodegenerative disease research. As a proof-of-principle, we uncovered new localizations of Aβ and pTau, including pTau-positive spine-like protrusions at the axon initial segment and changes in the number and size of synapses near Aβ plaques. Our vCLEM approach facilitates the discovery of both molecular and structural alterations within large-scale EM data, advancing connectomics research in Alzheimer's and other neurodegenerative diseases.

Keywords

Alzheimer's disease, Aβ, tau, nanobody, volume electron microscopy, connectomics, correlated light and electron microscopy

Introduction

Alzheimer's disease (AD) and related dementias are escalating global health crises, affecting over 6 million people in the U.S., with care costs projected to surpass $1 trillion annually by 2050 ("2024 Alzheimer's Disease Facts and Figures" 2024). The annual incidence of dementia is expected to nearly double by 2060, underscoring the urgent need to uncover mechanisms underlying AD pathology and develop more effective treatments (M. Fang et al. 2025). Despite decades of research targeting pathological markers such as amyloid-β (Aβ) and hyperphosphorylated tau (pTau), most therapeutic efforts have achieved only modest efficacy (Cummings et al. 2024).

Traditional studies of AD often focus on isolated aspects—gene expression changes, protein alterations, or synaptic density—without capturing how these abnormalities interact within neuronal networks, a key driver of cognitive impairments (Yu, Sporns, and Saykin 2021). The field has been asking for integrative approaches that can access perturbation of the diseases at molecular, cellular as well as anatomical levels (Urbanski et al. 2019; Wood, Winslow, and Strasser 2015). Volume electron microscopy (volume EM) (Peddie et al. 2022)-based connectomics (Swanson and Lichtman 2016) offers a transformative framework for studying these interactions by providing nanoscale insights into neuronal and synaptic organization while simultaneously revealing cellular and subcellular pathology. This approach, while not yet extensively applied to AD, has been used in human tissue studies (Loomba et al. 2022; Shapson-Coe et al. 2024; Karlupia et al. 2023) and holds promise for advancing AD research.

Volume EM techniques, such as focused ion beam-scanning electron microscopy (FIB-SEM) (Knott et al. 2008), have provided valuable insights into synapse morphology and density in AD samples (Montero-Crespo et al. 2021; Domínguez-Álvaro et al. 2018; Blazquez-Llorca et al. 2013). However, their limited imaging volume (~10 μm^3) restricts the study of larger networks. Advances in ATUM-SEM (Hayworth et al. 2006; Kasthuri et al. 2015) and TEMCA (Lee et al. 2016) have enabled datasets on the millimeter scale, encompassing thousands of neurons and more comprehensive circuits (MICrONS Consortium et al. 2021; Loomba et al. 2022; Motta et al. 2019; Sievers et al. 2024; Nguyen et al. 2022; Kuan et al. 2024; Shapson-Coe et al. 2024). Yet, datasets specific to AD remain small and fragmented, hindering a holistic understanding of the disease. A hybrid method, ATUM-FIB, combines large-scale context information with local high-resolution FIB volumes and has been applied to samples from the AD

83 mouse model 5xFAD (Kislinger, Fabig, et al. 2023). Despite these advancements, existing Alzheimer's
84 datasets remain small and fragmented, with the largest ATUM-SEM dataset for AD models covering only
85 ~45,000 cubic microns (Jiang et al. 2022; Pang et al. 2022; Kislinger, Niemann, et al. 2023). The scarcity
86 of larger-scale vEM datasets restricts the ability to comprehensively analyze and interpret alterations in
87 neuronal networks and cellular structures, which are critical for understanding the mechanisms of AD and
88 related dementias.

89 In addition to neuronal connectivity disruptions, AD is characterized by pathological protein
90 aggregates, including amyloid-β (Aβ) (Taylor, Hardy, and Fischbeck 2002; G.-F. Chen et al. 2017) and
91 hyperphosphorylated tau (pTau) (Mandelkow and Mandelkow 1998; Noble et al. 2013) in the brain
92 parenchyma. Despite their importance, there is very limited knowledge of how these hallmark pathological
93 proteins exhibit distinct and identifiable ultrastructural features in EM datasets, making additional
94 molecular labeling essential for their reliable detection. Extracellular Aβ accumulates into dense-core or
95 diffuse plaques, which are detectable by EM (Blazquez-Llorca et al. 2013), while intracellular Aβ—
96 potentially more neurotoxic than plaques—has also been identified (Gouras et al. 2010; LaFerla, Green,
97 and Oddo 2007; Kelly et al. 2021). However, the precise manifestation of intracellular Aβ in EM images
98 remains elusive, underscoring the importance of complementary molecular techniques. Similarly, pTau
99 aggreagtes, identifiable by TEM as either straight or paired helical filaments (Crowther 1991), localize to
100 cytoplasm, dendrites, and axons. Soluble forms of pTau are considered more neurotoxic than aggregates
101 (Noble et al. 2013), yet whether either form exhibits specific ultrastructural characteristics detectable in
102 ATUM-SEM data remains uncertain. These gaps highlight the critical need for innovative molecular
103 labeling strategies to advance the study of AD pathology within large-scale EM datasets. Traditional
104 methods for detecting these proteins often rely on detergents, which compromise sample ultrastructure
105 (Im et al. 2019). Advanced labeling techniques are necessary to localize these pathological proteins
106 reliably while preserving ultrastructure.

107 To address these challenges, we employed volumetric correlated light and electron microscopy
108 (vCLEM), combining detergent-free immuno-probe (nanobody or single-chain variable fragment, scFv) -
109 assisted immunofluorescence with large-scale ATUM-SEM imaging (T. Fang et al. 2018; Han et al. 2024).
110 Nanobodies and scFvs, being only one-tenth or one-fifth the size of full-length IgG antibodies (see Figure

111 1 a for nanobody), exhibit excellent diffusion properties, enabling efficient labeling of intracellular proteins
112 without requiring detergents. This approach preserves the ultrastructure of the sample (compare Figures
113 1 b and 1 c) and allows the labeling of multiple proteins in thick, unpermeabilized tissue. The labeled
114 protein localizations can then be superimposed onto EM data generated by ATUM-SEM from the same
115 sample, providing a powerful tool to directly link protein alterations to connectomic data. Despite its
116 potential, vCLEM techniques have not yet been applied to AD or other dementia-related samples to
117 facilitate research into these diseases.

118 In this study, we leveraged the vCLEM technique to localize Aβ and pTau in the hippocampal
119 CA1 region of a female 3xTg AD model mouse. We developed two fluorescent nanobody probes
120 targeting Aβ and pTau, which proved effective for detergent-free immunofluorescence. Alongside
121 additional probes for microglia/macrophages (CD11b), astrocytes (GFAP), and blood vessels (Ly-6C/6G),
122 these enabled precise molecular labeling of thick, unpermeabilized brain tissue. Using this approach, we
123 generated and share a large-volume ATUM-SEM-based connectomics dataset with preserved
124 ultrastructure, integrating molecular and structural information. In the dataset, we were able to localize
125 extracellular Aβ plaques, intracellular Aβ and pTau at various novel locations.

126 Machine learning-based segmentation, including style transfer (Michał Januszewski et al. 2018;
127 Michal Januszewski and Jain 2019) and supervised learning (Lin et al. 2021), facilitated automatic
128 segmentation of neurons, dendrites, axons, glial processes, and synapses. The fully segmented dataset,
129 now publicly accessible, supports 3D reconstruction of neurons, glia, their compartments, and synapses.
130 Importantly, it is designed to be user-friendly for researchers in the AD field who may not be familiar with
131 volume EM-based connectomics, enabling detailed analyses of cellular and network alterations. As a
132 proof of principle, we identified previously unreported pTau localizations in enlarged, spine-like structures
133 at the axon initial segment and observed synaptic changes surrounding an Aβ plaque. These findings
134 highlight the potential of our dataset to uncover novel pathologies at molecular, cellular, and circuit levels.
135

136 ## Results

137 ### Generation of fluorescent nanobody probes for detergent-free immunolabeling of pTau and Aβ

138 To verify that detergent-free immunolabeling using nanobodies can localize pTau and Aβ in a

139 vCLEM-compatible manner, we adapted two previously developed and validated nanobodies— A2, which
140 specifically binds tau protein phosphorylated at multiple sites including S422; R3VQ, which selectively
141 binds Aβ40/42 without cross-reacting with amyloid precursor protein (APP), the precursor from which Aβ
142 is derived (T. Li et al. 2016; Lafaye et al. 2019, 2020)—into fluorescent probes (see Table 1). To facilitate
143 broader use, we designed expression plasmids of these two nanobodies, optimized for easy, high-yield
144 purification by Expi 293 cells and direct fluorescent dye conjugation (see Methods). These plasmids have
145 been deposited at Addgene, and we provide a step-by-step protocol (Sup. File 1) to enable the
146 generation of these probes.

147 **Table 1. Fluorescent nanobody immuno-probes generated in this work.**

Target	Clone No.	Source	Fluorescent dyes conjugated	Link for expression plasmid at Addgene
pTau	A2	(Li et al. 2016)	5-TAMRA, Alexa Fluor 594, Alexa Fluor 647	https://www.addgene.org/233218/
Aβ 40/42	R3VQ	(Li et al. 2016)	5-TAMRA, Alexa Fluor 647	https://www.addgene.org/233217/

148

149 We tested two red fluorescent (5-TAMRA-conjugated) A2 and R3VQ probes using our detergent-
150 free immunofluorescence protocol (see Methods) on tissue sections from the hippocampus CA1 region of
151 3xTg mice that preserves fine ultrastructure and is compatible with vCLEM (Compare Figure 1 b and c).
152 This AD mouse model shows neurofibrillary tangles formed by pTau, Aβ extracellular plaques and
153 intraneuronal Aβ deposits (Oddo et al. 2003).The A2 probe selectively labeled neurofibrillary tangle
154 (NFT)-like structures in the cell bodies and dendrites of certain neurons (Figure 1 d-1, d-2; Sup. Fig. 1), as
155 well as the dystrophic neurites nearby plaque material (Figure 1 e-1, e-2; ; Sup. Fig. 1). The R3VQ probe
156 selectively labeled extracellular plaques (Figure 1 f-1, f-2; ; Sup. Fig. 1) and the cell bodies of certain
157 neurons (Figure 1 g-1, g-2; ; Sup. Fig. 1).

158 Interestingly, we also observed R3VQ labeling in neuronal nuclei within neurons showing
159 intracellular R3VQ signal (Figure 1 g-1, g-2; ; Sup. Fig. 1 e). While nuclear localization of Aβ is not widely
160 established, a few reports suggest it may occur under certain conditions (Barucker et al. 2014; D'Andrea

161 et al. 2021). However, given that prolonged fixation with glutaraldehyde was used in our protocol to
162 preserve ultrastructural, this nuclear signal could also be an artifact of fixation-induced autofluorescence
163 or redistribution of Aβ. Further investigation, such as alternative fixation protocol and colabeling
164 approaches, would be required to clarify this observation.

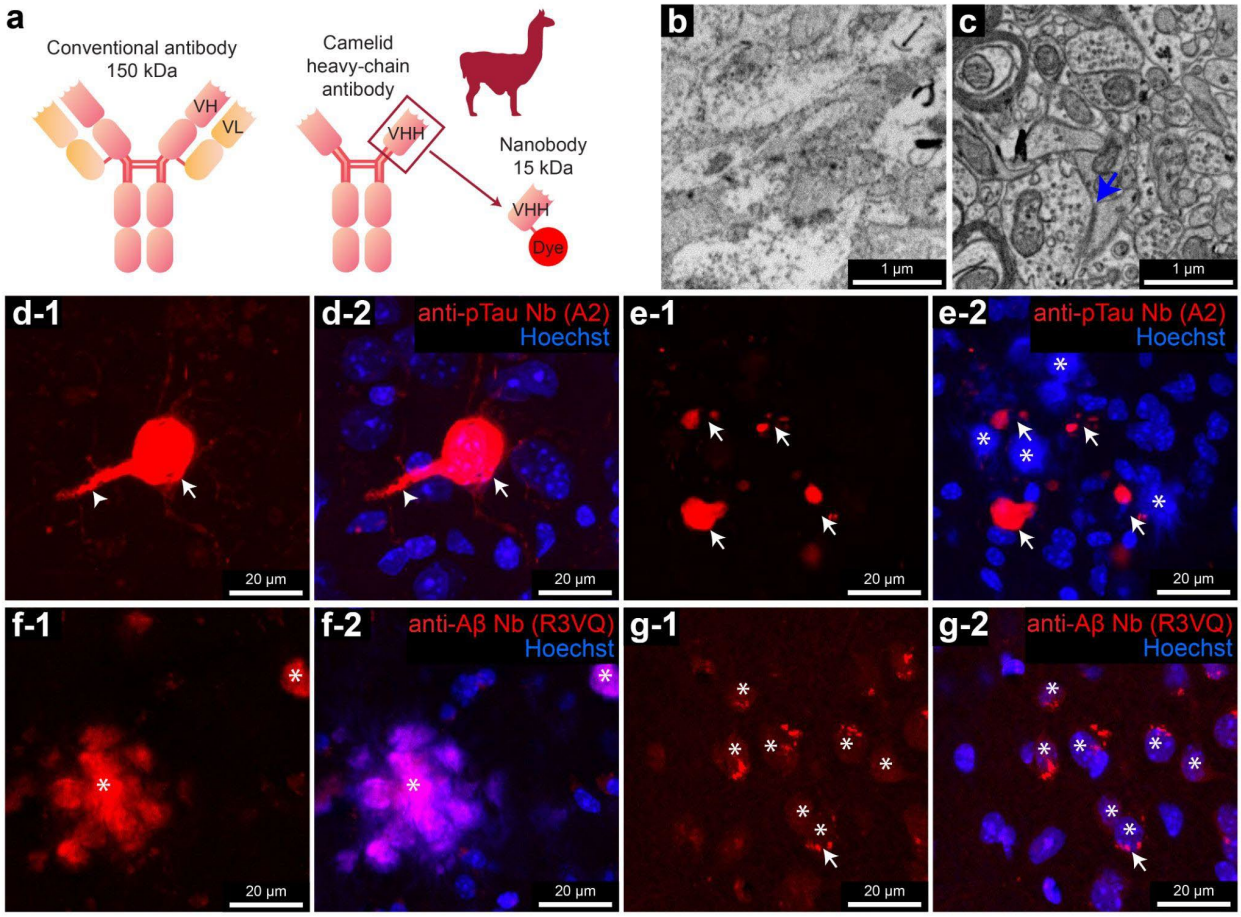

165

166 **Figure 1. Characterization of fluorescent nanobody probes for pTau and Aβ.**

167 **a**, Schematic representations of a full-length IgG antibody, a camelid antibody, and a nanobody probe
168 with a conjugated fluorescent dye. **b**-**c**, Comparison of ultrastructure between a sample (**b**) treated by
169 Triton X-100 and a sample (**c**) labeled by nanobody probes, untreated with Triton X-100. Blue arrow in **c**
170 indicates a synapse. **d-1** to **e-2**, Confocal images from the hippocampus of a 3xTg mouse labeled with a
171 pTau-specific nanobody probe (A2) conjugated with the red dye 5-TAMRA. The panels **d-1**, **e-1** only
172 show the nanobody labeling. Arrows in **d-1** and **d-2** show the labeled neuronal cell body. Arrowheads in
173 **d-1** and **d-2** show the labeled apical dendrite. Arrows in **e-1** and **e-2** show the labeled neurites. Asterisks
174 in **e-2** show extracellular plaque material labeled by Hoechst, as reported before (Uchida and Takahashi
175 2008). **f-1** to **g-2**, Confocal images from the hippocampus of a 3xTg mouse labeled with an Aβ-specific
176 nanobody probe (R3VQ) conjugated with the red dye 5-TAMRA. The panels **f-1**, **g-1** only show the
177 nanobody labeling. Asterisks in **f-1** and **f-2** show the labeled plaque material. Asterisks in **g-1** and **g-2**
178 show the labeled neuronal cell bodies. Arrows in **g-1** and **g-2** show the autofluorescent lipofuscin.
179
180 Double immunofluorescence using A2 and anti-pTau mAb AT8, and R3VQ and anti-Aβ mAb 4G8

181 confirmed colocalization of signals (Sup. Figure a-1 to a-3, b-1 to b-3). No labeling was detected with A2
182 or R3VQ in sections from age-matched control animals (Sup. Figure 1 d and f). These results
183 demonstrate that these fluorescent nanobody probes can localize Aβ and pTau in a detergent-free
184 immunolabeling approach compatible with vCLEM.

185 Leveraging the flexibility of our protocol for easy conjugation of different fluorophores to the
186 nanobodies, a broader application of these probes is for multiplex detergent-free immunolabeling. As a
187 proof-of-principle, we combined these two probes with three additional nanobody probes for multiplex
188 detergent-free immunolabeling. In one set of experiments, We used three fluorescent nanobody probes
189 (A2, R3VQ, and anti-CD11b) to label two 120-μm thick brain sections in the absence of detergent (Figure
190 2 a, b; see Sup. Figure 2 for the anatomical details of the labeled sections) of a one-year-old female 3xTg
191 mouse. CD11b is a marker for myeloid cells, including microglia and macrophages in the brain
192 parenchyma (Bisht et al. 2016; Sedgwick et al. 1991; Martin et al. 2017). We acquired a four-color
193 fluorescence 57-μm image stack (Figure 2 a) from the first section and a 21-μm stack from the second
194 section (Figure 2 b; see Sup. Figure 2 for the anatomical details of the imaged regions of interest) in the
195 stratum pyramidale in the CA1 region of the hippocampus. In both image stacks, NFT-like structures in
196 the cell bodies and dendrites of certain pyramidal neurons and some dystrophic neurites were labeled by
197 the anti-pTau probe (yellow signals in Figure 2 c, d). In addition, intraneuronal Aβ of certain pyramidal
198 neurons were labeled by the anti-Aβ probe (magenta signals in Figure 2 c, d). Microglia/macrophages
199 were labeled by the anti-CD11b probe (green signals in Figure 2 c, d). We noted that these labeled
200 structures/cells were more abundant, and the labeled apical dendrites appeared to be more tortuous in
201 the image stack acquired from the more caudal section (Figure 2 c, d). Only in this image stack (Figure 2
202 a, c) did we find five extracellular Aβ plaques labeled by the anti-Aβ 40/42 probe (magenta signals in
203 Figure 2 a, c). These findings are consistent with the fact that the pathologies of neurofibrillary tangles
204 and Aβ plaques progress from caudal to rostral in the hippocampus in the 3xTg mice (Belfiore et al.
205 2019).

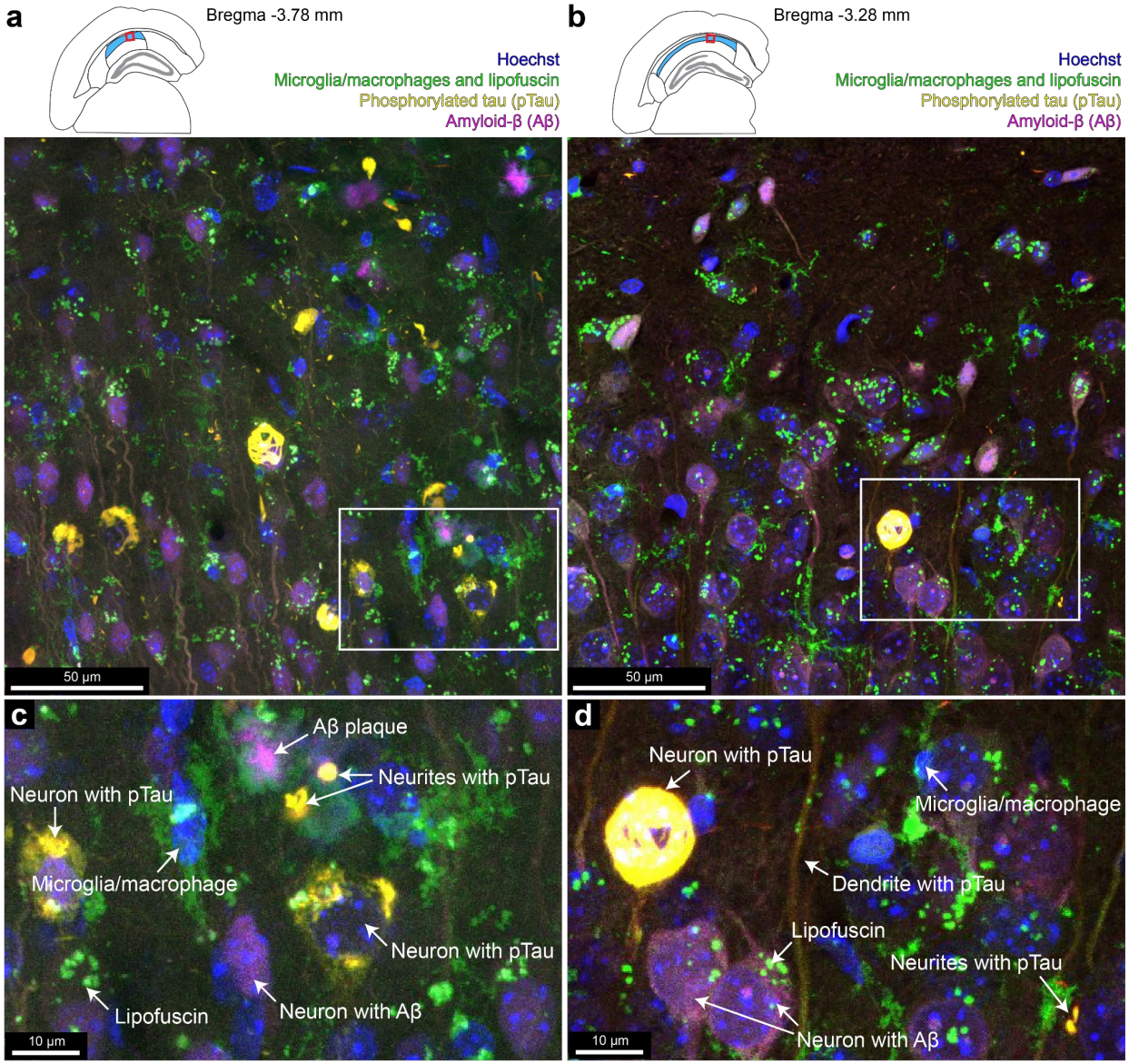

Figure 2. Four-color detergent-free immunofluorescence enabled by nanobody probes.

Maximum intensity projection of the multi-color fluorescence image stacks acquired from the hippocampus at the Bregma -3.78 mm (**a**) or the Bregma -3.28 mm (**b**) of a 3xTg mouse labeled with a CD11b-specific nanobody probe conjugated with Alexa Fluor 488, a pTau-specific nanobody probe conjugated with 5-TAMRA, and an Aβ-specific nanobody probe conjugated with Alexa Fluor 647. Red boxes in the coronal section illustrations show where the image stacks were acquired. The stratum pyramidale of the hippocampal CA1 region is labeled in blue in the illustrations. **c**-**d**, enlarged boxed insets from **a**-**b**. Because the red fluorescence signal from the anti-pTau probe was far stronger than the green signal from the anti-CD11b probe, we saw crosstalk in the green channel. This meant that in the overlay, the pTau label appears yellow whereas the microglia appear green, but the two labels were nonetheless unambiguous. Another issue was that aged mice have lipofuscin particles in cell bodies of neurons and glia. This non-specific fluorescence localized to inclusion bodies that were easily differentiated from the membrane labeling of microglia.

In another experiment, we used four fluorescent nanobody probes (A2, anti-CD11b, anti-GFAP,

222 and anti-Ly-6C/6G) to label a 120-μm thick brain section at Bregma -3.78 mm of another one-year-old
223 female 3xTg mouse in the absence of detergent. Ly-6C is a lymphocyte antigen expressed by circulating
224 monocytes recruited to sites of inflammation and endothelial cells of blood vessels (Martínez-Carmona et
225 al. 2021; Mildner et al. 2007). We acquired a five-color fluorescence image stack of 23 μm (Figure 3).
226 Numerous activated astrocytes, labeled by the anti-GFAP nanobody probe, were observed nearby
227 extracellular plaque material and neurons/neurites containing pTau (yellow signals in Figure 3 a, b).
228 Interestingly, the anti-Ly-6C/6G nanobody labeled not only blood vessels but also some, though not all,
229 plaque material (white arrows in Figure 3 d), which was surrounded by microglia/macrophages marked by
230 the anti-CD11b probe (green signals in Figure 3 d). Since Ly-6C labels monocytes recruited to
231 inflammation sites, which differentiate into macrophages also expressing CD11b (Mildner et al. 2007), it is
232 likely that the CD11b-positive cells surrounding plaques are macrophages derived from monocytes, rather
233 than resident microglia.

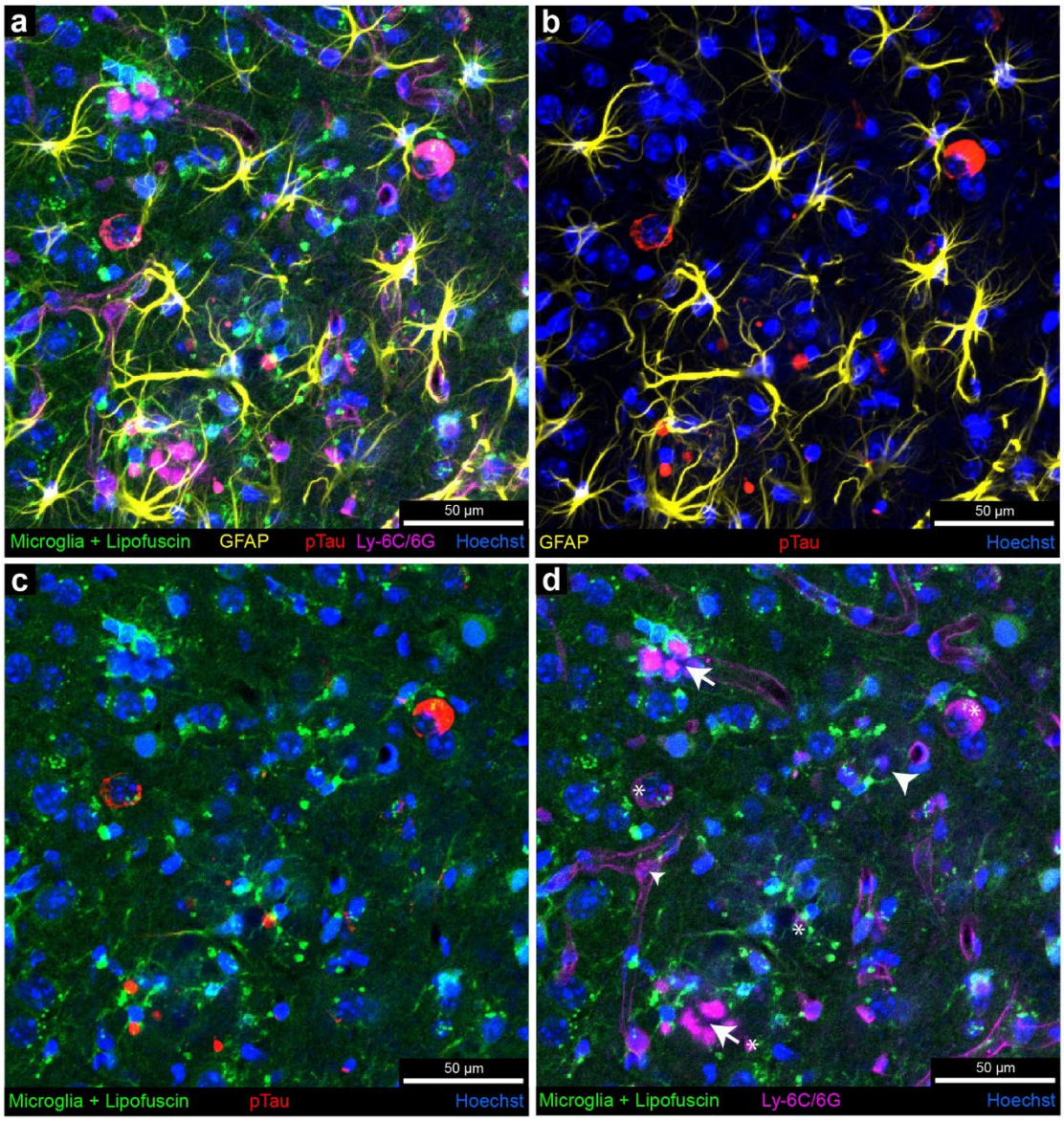

Figure 3. Five-color detergent-free immunofluorescence enabled by nanobody probes.

a, Maximum intensity projection of the multi-color fluorescence image stacks acquired from the hippocampus of a 3xTg mouse labeled with a CD11b-specific nanobody probe conjugated with Alexa Fluor 488, a GFAP-specific nanobody probe conjugated with 5-TAMRA, a pTau-specific nanobody probe conjugated with Alexa Fluor 594, and a Ly-6C/6G-specific nanobody probe conjugated with Alexa Fluor 647. The signal of each fluorescent dye was pseudo-colored for better visualization. **b-d**, Three-channel maximum intensity projection images of the multi-color fluorescence image stack. White arrows in **d** show the labeled plaque material by the anti-Ly-6C/6G nanobody probe. The arrowhead shows plaque material not labeled by the anti-Ly-6C/6G nanobody probe. Asterisks show the crosstalk signals from the anti-pTau labeling.

Multi-color, large-scale vCLEM dataset with nanobody labeling, segmented neurons, glia and synapses

From the section shown in Figure 2 a, we acquired a high-resolution vEM dataset measuing 245 µm x 238 µm x 23 µm at a resolution of 4 nm x 4 nm x 30 nm (Figure 4 a) through ATUM-multi-SEM (see Methods). To the best of our knowledge, this represents the largest vEM volume obtained from an AD mouse model. Notably, the ultrastructure was well preserved across the entire volume, attributed to the exclusion of detergents during labeling, enabling the clear identification of various types of synapses (Figure 4 b, blue arrows).

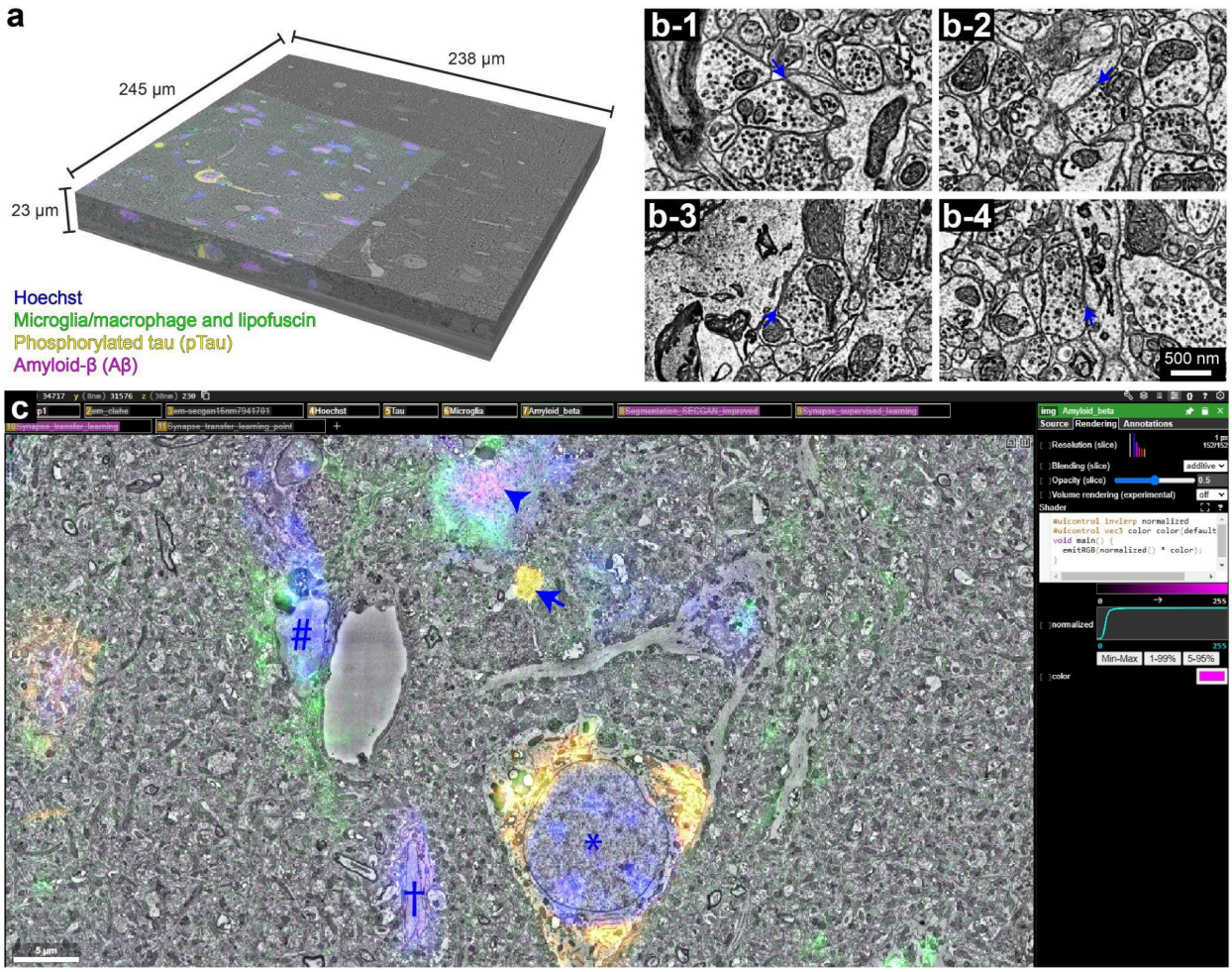

Figure 4. The four-color vCLEM dataset reveals ultrastructural abnormalities that colocalize with nanobody labeling.

a, The high-resolution vEM volume acquired from the hippocampus CA1 region with four-color immunofluorescence from nanobody probes. The four-color fluorescence data was co-registered with the high-resolution vEM data. **b-1** to **b-4**, the preserved ultrastructure from this vEM volume. The blue arrows

260 show synapses on a dendritic spine head (**b-1**), a dendritic shaft (**b-2**), a neuronal cell body (**b-3**), and an
261 axon initial segment (**b-4**). **c**, Visualization of the vCLEM dataset in the Neuroglancer interface, overlaying
262 fluorescence and EM ultrastructure. The asterisk indicates the cell body of a pyramidal neuron labeled by
263 the anti-pTau nanobody. The arrow indicates the dystrophic neurite labeled by the anti-pTau nanobody.
264 The arrowhead indicates the plaque material labeled by the anti-Aβ nanobody. The obelisk indicates the
265 cell body of a pyramidal neuron labeled by the anti-Aβ nanobody. The hash mark indicates the microglia
266 labeled by the anti-CD11b nanobody. This region corresponds to the one shown in Figure 2 c.
267
268 To enable the precise co-registration between the confocal fluorescence volume and the vEM
269 dataset for generating a vCLEM dataset, the heavy-metal-stained, resin-embedded section was scanned
270 by X-ray CT (microCT) (see Methods) prior to ATUM sectioning. The microCT image volume revealed
271 regions with Aβ plaques and neuronal degeneration consistent with previous report (Barbone et al.
272 2022)(Sup. Figure 3). High-precision co-registration between the fluorescence volume and the vEM
273 dataset was achieved by identifying corresponding landmarks, such as blood vessels and cell nuclei,
274 across both volumes. We employed the FIJI/ImageJ plugin BigWarp (Bogovic et al. 2016) to perform a 3D
275 transformation of the fluorescence volume via thin-plate spline interpolation to co-register the volumes.
276 The transformed fluorescence volume, overlaid onto more than one-third of the high-resolution EM
277 volume, is shown in Figure 4 a. This co-registration allows for the precise localization of fluorescence
278 signals from each nanobody labeling within EM ultrastructure. In Figure 4 c, a representative region
279 demonstrates that pTau (yellow) overlaps with the cell body of a pyramidal neuron and a dystrophic
280 neurite, Aβ (magenta) associates with an Aβ plaque and the cell body of another pyramidal neuron, and
281 CD11b (green) localized to a microglial cell/macrophage. We ingested this vCLEM dataset into
282 Neuroglancer (Jeremy Maitin-Shepard, et al.), providing a publicly accessible link for users to visualize
283 the fluorescence and the EM channels, either separately or in combination, and navigate through slices at
284 different resolution levels (Figure 4 c; Video 1).
285 Efficient connectomic analysis of large vEM dataset critically depends on the rapid and accurate
286 segmentation of image data. We employed flood-filling networks (FFNs) (Michał Januszewski et al. 2018)
287 trained on a human cortex dataset (Shapson-Coe et al. 2024). While the direct application of the pre-
288 trained FFNs was sufficient for segmenting neuronal cell bodies and dendrites, it performed suboptimally
289 for segmenting axonal and glial processes (Sup. Figure 4 a). To address this, we utilized Segmentation
290 Enhanced CycleGANs (Michal Januszewski and Jain 2019) to adjust the visual appearance of this data to
291 more closely match the H01 dataset prior to segmentation. This approach substantially improved the

292 segmentation of axonal and glial processes (Sup. Figure 4 b; Figure 5 a). The updated segmentation
293 results are also publicly available as a segmentation layer ("Segmentation_SECGAN_improved") through
294 the previously mentioned link. Users can perform 3D reconstructions of neuronal or glial cells by manually
295 agglomerating segments, simply by selecting the automatically generated segments associated with the
296 target cell (Figure 5 c; Video1).

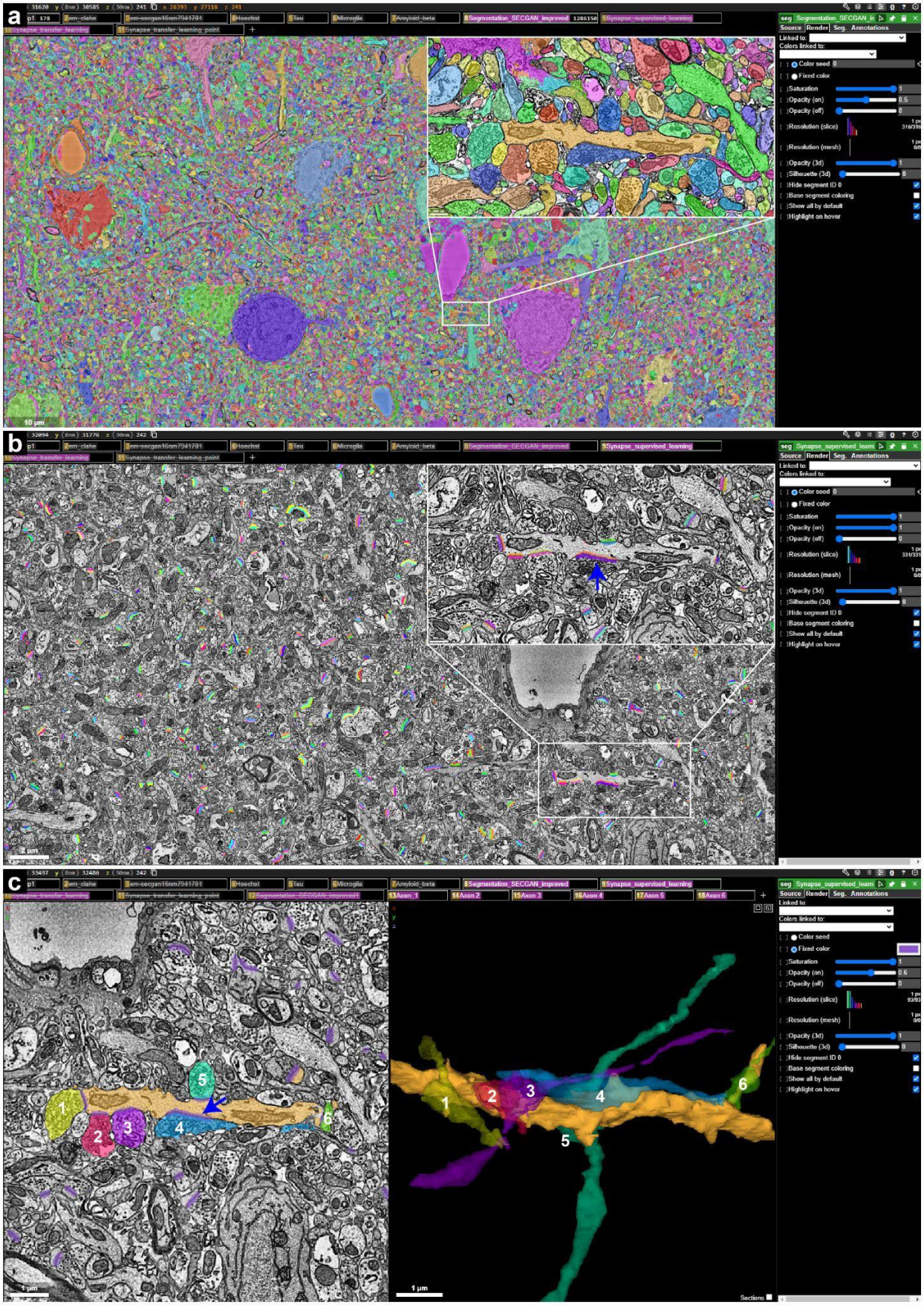

297

Figure 5. Efficient 3D reconstruction and synapse identification in the vCLEM dataset using segmentation and synapse prediction layers.

a, Visualization of the 3D segmentation layer ("Segmentation_SECGAN_improved") in the Neuroglancer interface. Each segmented object is uniquely color-coded, and users can click on these objects to reconstruct them in 3D. **b**,Synapse prediction layer ("Synapse_supervised_learning") visualized in Neuroglancer. Synapses are labeled with distinct colors for pre-synaptic (e.g., purple) and post-synaptic (e.g., orange) appositions. The blue arrow highlights a synapse located on a dendritic shaft. Users can click on these appositions to view their 3D structure. **c**, Example 3D reconstruction of a dendrite (orange) and six axonal profiles (numbered 1–6, each with a distinct color) using the segmentation and synapse prediction layers. Synapses formed by these axons are shown in purple. The blue arrow points to synapses made by axon No. 4.

Another key requirement for connectomic analysis is the comprehensive annotation and segmentation of all synapses. This is particularly crucial in AD studies, given the well-documented synaptic alterations (Scheff and Price 2006; Montero-Crespo et al. 2021, 2020) and the observed correlation between cognitive decline and reduced synapse density (DeKosky and Scheff 1990; Davies et al. 1987; Tzioras et al. 2023). Our vCLEM dataset offers the necessary resolution to precisely locate and analyze synapses at the ultrastructural level (Figure 4 b-1 to b-4). While manual annotation for synapse analysis is straightforward, it is not feasible for large-scale studies. Machine-learning-based automated synapse detection (Çiçek et al. 2016; Parag et al. 2019; Lin et al. 2021; Buhmann et al. 2021) has been successfully applied to large-scale connectomics datasets (Shapson-Coe et al. 2024; Turner et al. 2022; Scheffer et al. 2020), demonstrating efficiency, objectivity, and accuracy.

For automatic synapse prediction, we employed the U-Net deep learning model (Parag et al. 2019) to identify the pre- and postsynaptic components of each synapse. Two approaches were explored: a supervised learning approach and a transfer learning approach, utilizing two existing synapse prediction frameworks (Lin et al. 2021; Shapson-Coe et al. 2024). For evaluation, we manually annotated all synapses within a small subvolume measuring 6 μm × 6 μm × 1.5 μm.

In the supervised learning approach, synapses were annotated within a randomly selected subvolume measuring 6 μm × 6 μm × 6 μm, distinct from the evaluation subvolume. This training dataset primarily consisted of neuropil and excluded regions containing blood vessels or cell bodies. Following the guidelines of an online tutorial (Lin et al. 2021), we trained the synapse prediction model and applied the watershed transform to convert the predictions into synapse instances (see Methods). On the evaluation subvolume, this model achieved a precision of 86.06% and a recall of 98.88%. Applied to the

entire dataset, the model identified approximately 3.5 million synapses. This first version of synapse predictions is publicly available via the aforementioned repository as an independent data layer ("Synapse_supervised_learning") (Figure 5 b). In this layer, each synapse is labeled with one presynaptic segment and one postsynaptic segment, assigned consecutive segment IDs (Figure 5 b). Users can identify synapses in EM images and visualize them in 3D by interacting with the corresponding segments (Figure 5 c; Video 1). Additionally, these 3D visualizations can be integrated with cell reconstructions for advanced analysis (Figure 5 c; Video 1).

While effective, the supervised approach missed many synapses due to the limited diversity in the small training dataset. To address this limitation, we adopted a transfer learning approach using a pretrained synapse prediction model developed for a human cortex dataset (Shapson-Coe et al. 2024). To adapt it to this dataset, we first ran the synapse models trained on the human cortex dataset on this data with SECGAN style-transfer applied to mimic the human dataset. This produced 0.225 million synaptic masks with low false positive rates, but with a significant number of false negatives (estimated at about 50%), particularly within neuronal processes (Sup Figure 5 a-1 to a-3) which require filtering. We then used these masks as model-produced ground truth to retrain the synapse model from scratch on this dataset without SECGAN. The retrained model produced synapses with significantly improved precision of 46% and recall of 52%. Applied to the entire dataset, the model's predictions were filtered to retain only synapses associated with neuronal membranes, resulting in the identification of approximately 0.7 million synapses. This second version of synapse predictions is also publicly available as a separate data layer ("Synapse_transfer_learning") (Sup Figure 5 b-2). Like the first version, it enables users to identify, visualize, and reconstruct synapses in 3D. This version proved particularly effective in detecting synapses missed by the supervised approach (Sup Figure 5 b-2), leveraging the pretrained model's knowledge of synapse morphology in the human cortex. Since both synapse detection layers are accessible in Neuroglancer, users can combine them, resulting in a union that achieves greater precision than either model alone. This dual-layer approach serves as a complementary resource for synapse identification and analysis, ensuring a more comprehensive and accurate mapping of synaptic structures.

The publicly accessible dataset is among the largest vEM datasets generated for an AD model, offering unique opportunities for the scientific community. With fully segmented neuronal and glial cells,

359 as well as synapses, it provides an invaluable resource for researchers, particularly those studying AD
360 and other dementias who may be less familiar with volume EM-based connectomics. This innovative
361 dataset enables the following: (1) pinpointing cells and cellular structures where Aβ and pTau are
362 localized using overlapping fluorescence signal layers; (2) reconstructing affected neurons and glial cells
363 at nanometer resolution with the 3D segmentation layer to understand how AD-related abnormalities
364 manifest in cellular morphology; (3) exploring how the localization of Aβ and pTau impacts synaptic
365 connectivity and neuronal networks using the synapse segmentation layer; (4) generating new
366 hypotheses based on findings from the dataset to be tested with other methodologies; and (5) comparing
367 findings with those reported in the literature or observed in other animal models or human tissues. By
368 lowering the barrier to entry for researchers unfamiliar with volume EM or segmentation tools, this dataset
369 fosters broader participation in connectomics-driven AD research and encourages cross-disciplinary
370 collaboration.

371 **vCLEM dataset uncovers ultrastructural pathologies that colocalize with nanobody labeling**

372 To demonstrate the potential of this dataset for advancing AD research, we conducted an
373 analysis of sites labeled with each of the three molecular markers (pTau, Aβ, CD11b). This analysis
374 revealed an array of previously uncharacterized ultrastructural abnormalities colocalize with each marker,
375 providing insights into molecular and structural pathology at the nanoscale. These findings, along with
376 their spatial coordinates in the dataset, are compiled in Table 2 and discussed in detail in the following
377 paragraphs, providing a valuable resource for further investigation. Researchers can leverage this dataset
378 for in-depth 3D reconstruction of affected cells and subcellular structures, enabling new avenues for
379 identifying and understanding AD-related pathology.

380 **Table 2. Ultrastructural Pathologies that Colocalize with Nanobody Labeling**

Label	Location Type	Subtype	Other Ultrastructural Property	Coordinates
pTau				
	Neuronal soma			
		Only pTau		
			pTau with straight filament	(26467, 24370, 155)

			pTau with no straight filament, but short-filamanet	(28449, 33128, 151), (35520, 32879, 177), (19278, 27572, 51), (20141, 28463, 466)
		Both pTau and A-beta		(30106, 31592, 365), (18693, 21208, 510)
	Dendrite			
		Straight		(25988, 27500, 121), (28382, 36337, 121), (35212, 35235, 142)
		Tortuous		(21209, 33200, 220), (25698, 33034, 266), (21539, 35309, 235)
	Axon			
		Bleb-like structure from AIS		(35464, 30205, 439), (34864, 30905, 460)
		Bleb-like structure from myelinated axon		(28612, 18697, 157)
		Swelling		(28301, 30383, 77)
	Glia			(32846, 20364, 661)
Aβ	Plaque			(34331, 29527, 215), (32240, 12443, 266), (36268, 27060, 438), (32071, 16340, 110), (39797, 13403, 748)
	Neuronal soma	Only Aβ		(23970, 30423, 166), (33496, 33578, 365)
CD11b	Cell associated with A-beta plaques			(32878, 30971, 183), (34740, 27790, 255), (33988, 28188, 7), (37528, 35367, 55), (36983, 26638, 404)
	Cell associated with dystrophic neurites			(24013, 20988, 186), (31741, 19684, 293), (37100, 25861, 659), (29528, 12771, 599)
	Cell adjacent to neuron with intraneuronal A-beta			(23113, 30303, 100)

*The coordinates can be entered into Neuroglancer as in Sup. Figure 6 to move to the location.

383 pTau: Our analysis revealed a diverse array of pTau labeling patterns across different
384 ultrastructural contexts, highlighting a complex landscape of pTau-associated abnormalities. We found
385 NFT-like structures from the labeling of the anti-pTau nanobody localized within cell bodies of seven
386 pyramidal neurons and one glial cell (red fluorescence, see Figure 6 a-1 to d-2 for four examples for
387 neurons, and j-1 and j-2 for the glial cell) among the ~100 neuronal and glial cells in the volume where the
388 fluorescence signals were co-registered. Only one of the seven pTau positive pyramidal cells (which did
389 not show intraneuronal Aβ), showed pathological straight filament-like structures (Figure 6 a-1, a-2; Sup.
390 Figure 7 a), which is one of the ultrastructural manifestations of neurofibrillary tangles (Crowther 1991).
391 The other pTau positive pyramidal cells showed short filament-like structures in their cell bodies (Figure 6
392 b-2, c-2). We suspect that these are not pathological because in other pyramidal neurons free of pTau
393 labeling, similar structures were seen (Sup. Figure 7 c-1, c-2). Two of the pyramidal cells also showed
394 intraneuronal Aβ (magenta fluorescence, see Figure 6 d-1, d-2 for one example). These two neurons had
395 the same morphological features as neurons that only had intraneuronal Aβ (see below). We also found
396 NFT-like structures localized in dendrites that were either straight or tortuous (Figure 6 e-1 to f-2). Again,
397 we did not find specific ultrastructural manifestations of the neurofibrillary tangle structures in these
398 dendrites despite them being pTau positive (Sup. Figure 7 d-1, d-2). We examined four axonal sites with
399 pTau labeling. Two of these sites consisted of pTau positive, bleb-like structures each filled with straight
400 filaments and stemmed from the axon initial segment of a pTau positive pyramidal neuron (see Figure 6
401 g-1, g-2; see Sup. Figure 7 b for one of them). Another site showed an enlarged pTau positive swelling
402 filled with lipofuscin granules near the axon initial segment of a different pTau positive pyramidal neuron
403 (Figure 6 h-1, h-2). The fourth side contained a large pTau positive bleb-like structure filled with
404 degenerating organelles, emerging from a myelinated axon (Figure 6 i-1, i-2), similar to what has been
405 seen previously (Gowrishankar et al. 2015). The labeled glial cell had glial inclusions known as “coiled
406 bodies” (Ferrer et al. 2024; T. Li et al. 2016) which were specifically labeled by the anti-pTau probe
407 (Figure 6 j-1, j-2). Based on our observation that not all pTau-labeled sites exhibited characteristic
408 ultrastructural features of neurofibrillary tangles (NFTs), we propose that certain NFT-like structures or
409 pTau aggregates may lack visible ultrastructural representations. This underscores the importance of
410 using correlative microscopy and labeling technique like ours to identify neurons harboring these

aggregates in EM micrographs, as they may otherwise go undetected.

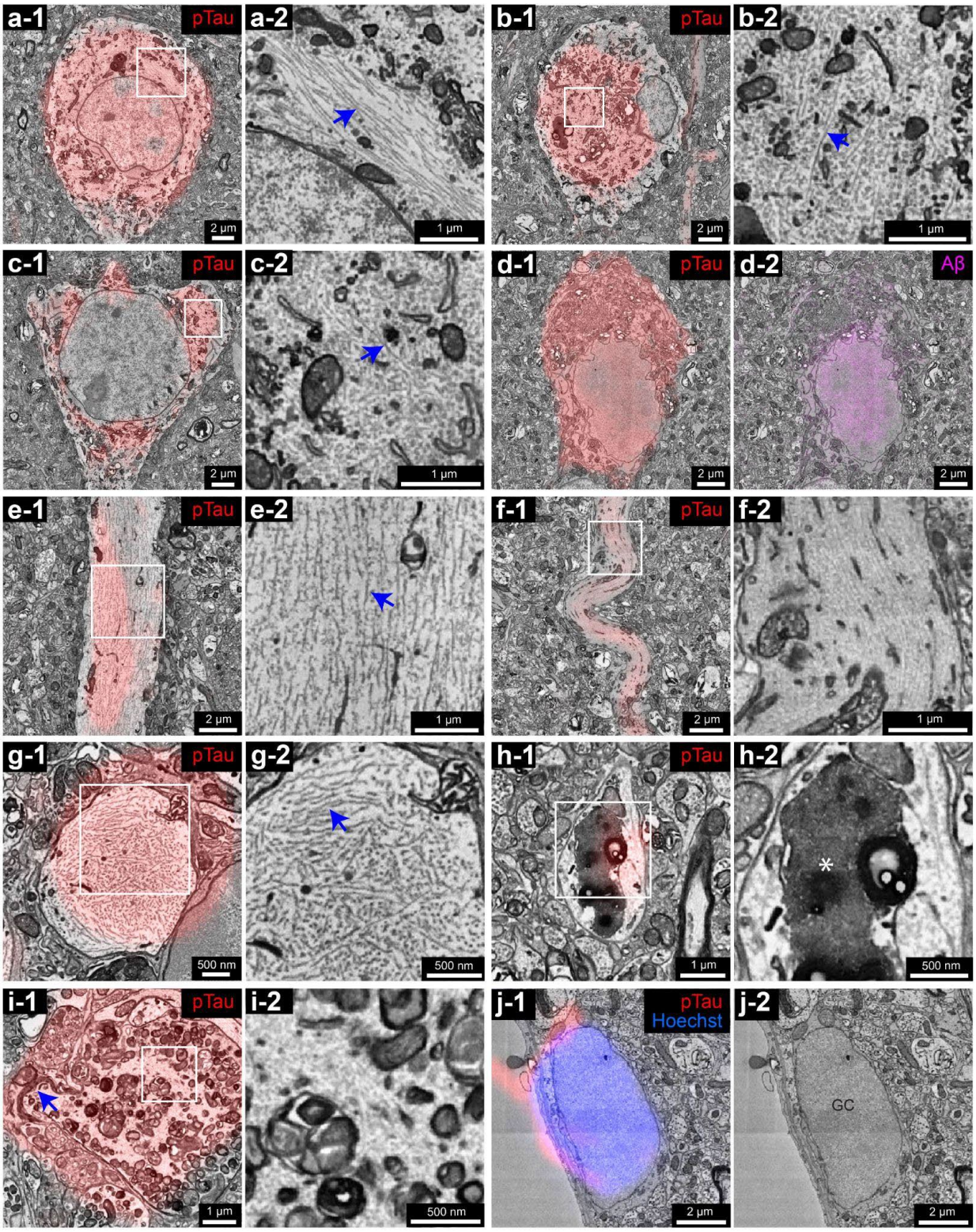

Figure 6. Ultrastructural abnormalities that colocalize with the labeling of pTau.

414 **a-1**, red fluorescence from the anti-pTau nanobody overlaps with the cell body of a pyramidal neuron. **a-2**,
415 enlarged inset from **a-1**. The blue arrow indicates the straight filament-like structure. **b-1** and **c-1**, red
416 fluorescence from the anti-pTau nanobody overlaps with the cell bodies of two pyramidal neurons. **b-2**
417 and **c-2**, enlarged insets from **b-1** and **c-1**. The red arrows indicate the short filament-like structures that
418 were also seen in neurons that were not labeled by the anti-pTau nanobody (see Sup. Figure 4 c-1, c-2).
419 **d-1** and **d-2**, the pyramidal neuron that was labeled by both the anti-pTau nanobody (red fluorescence in
420 **d-1**) and the anti-Aβ nanobody (magenta fluorescence in **d-2**). **e-1** and **f-1**, red fluorescence from the anti-
421 pTau nanobody overlaps with a straight apical dendrite and a tortuous apical dendrite of two pyramidal
422 neurons. **e-2** and **f-2**, enlarged insets from **e-1** and **f-1**. The blue arrow in **e-2** indicates the short filament-
423 like structure that was also seen in the apical dendrite that was not labeled by the anti-pTau nanobody
424 (see Sup. Figure 4 d-1, d-2). **g-1**, red fluorescence from the anti-pTau nanobody overlaps with a bleb-
425 structure connected to an axon. **g-2**, enlarged inset from **g-1**. The blue arrow indicates the straight
426 filament-like structure. **h-1**, red fluorescence from the anti-pTau nanobody overlaps with an enlarged
427 swelling of an axon filled with lipofuscin granules. **h-2**, enlarged inset from **h-1**. The asterisk shows the
428 lipofuscin granules. **i-1**, red fluorescence from the anti-pTau nanobody overlaps with a bleb-like structure
429 that emerged from a myelinated axon. This bleb was filled with degenerating organelles. The blue arrow
430 indicates the end of the myelination. **i-2**, enlarged inset from showing the degenerating organelles. **j-1**
431 and **j-2**, red fluorescence from the anti-pTau nanobody overlaps with a glial cell that had coiled bodies
432 (red fluorescence in **j-1**).
433
434 Aβ: We found extracellular Aβ plaque structures from the labeling of the anti-Aβ nanobody
435 (magenta fluorescence in Figure 7) localized within five separate spots of plaque material (see Figure 7 a-
436 1 to b-2 for two examples) which showed the typical ultrastructure of dense-cored plaques (Blazquez-
437 Llorca et al., 2013). These plaques had dense cores of Aβ deposits in the center, Aβ fibrils, glial
438 processes and dystrophic neurites surrounding them. Intraneuronal Aβ localized within neurons that had
439 very tortuous apical dendrites, shrunken cell bodies, dark osmiophilic cytoplasm and degenerating
440 organelles (Figure 7 c-1 to d-2). These neurons with intraneuronal Aβ appeared to be more abnormal
441 than neurons that only had pTau.

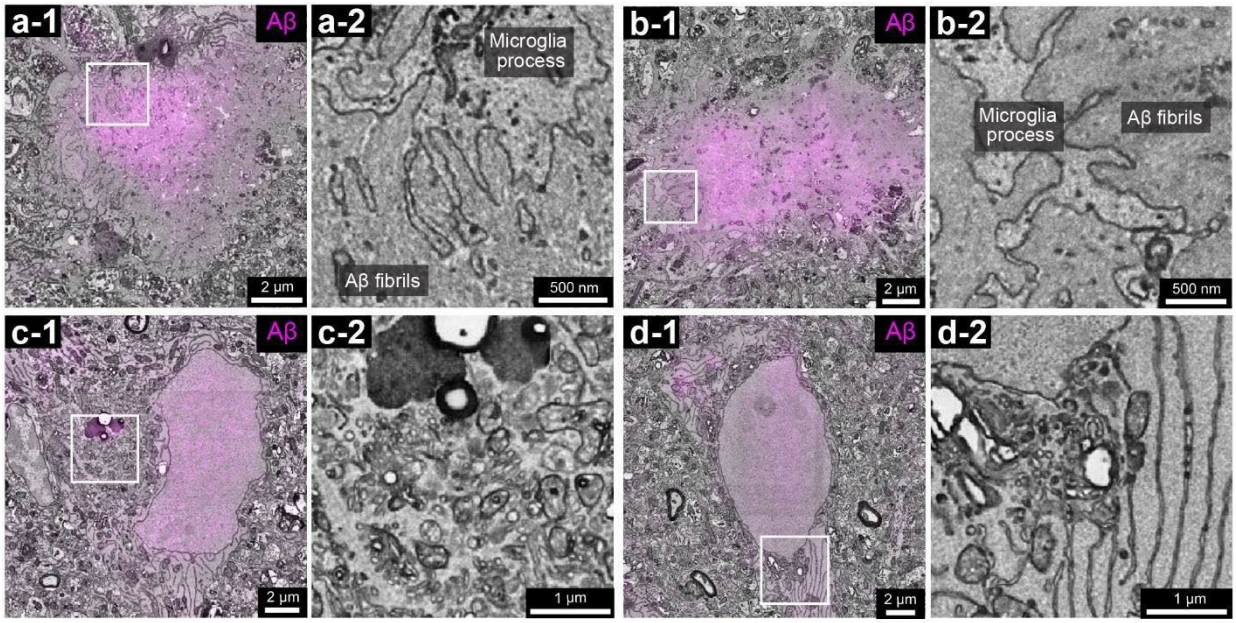

Figure 7. Ultrastructural abnormalities that colocalize with the labeling of Aβ.

a-1, magenta fluorescence from the anti-Aβ nanobody overlaps with plaque material. **a-2**, enlarged inset from **a-1**. **b-1**, magenta fluorescence from the anti-Aβ nanobody overlaps with another plaque material. **b-2**, enlarged inset from **b-1**. **c-1**, magenta fluorescence from the anti-Aβ nanobody overlaps with the cell body of a pyramidal neuron. **c-2**, enlarged inset from **c-1** showing the degenerating organelles in this neuron. **d-1**, magenta fluorescence from the anti-Aβ nanobody overlaps with the cell body of another pyramidal neuron. **d-2**, enlarged inset from **d-1** showing the dilated endoplasmic reticula in this neuron.

CD11b: CD11b is a myeloid cell marker that labels both resident microglia and infiltrating macrophages within the brain parenchyma (Sedgwick et al. 1991; Martin et al. 2017). As a component of the phagocytic receptor CR3, CD11b is present on the plasma membrane of glial processes that surround synaptic elements (Bisht et al. 2016). Among these cells, some microglia, characterized by a condensed, electron-dense cytoplasm and nucleoplasm, were referred to as 'dark microglia' in a previous electron microscopy studies (Bisht et al. 2016; St-Pierre et al. 2022). In our vCLEM dataset, we identified ten labeled cells based on anti-CD11b nanobody labeling (green fluorescence in Figure 8; five examples shown), although we could not distinguish between microglia and macrophages. Among them, five were associated with Aβ plaques (Figure 8 a-1, c-3, c-4), extending ramified processes to encircle and perhaps phagocytose plaque material (Figure 8 b); four however were associated with dystrophic neurites where there was no Aβ plaque (Figure 8 c-1); one was adjacent to a neuron that had intraneuronal Aβ (Figure 8 c-2). These cells appeared stressed: they had a large amount of lipofuscin granules, osmiophilic

463 cytoplasm, altered mitochondria, condensed nucleoplasm, and dilated endoplasmic reticulum (Figure 8 a-
464 2, a-3), which may be attributed to the activation of the integrated stress response (ISR) as previously
465 described (Flury et al. 2024).

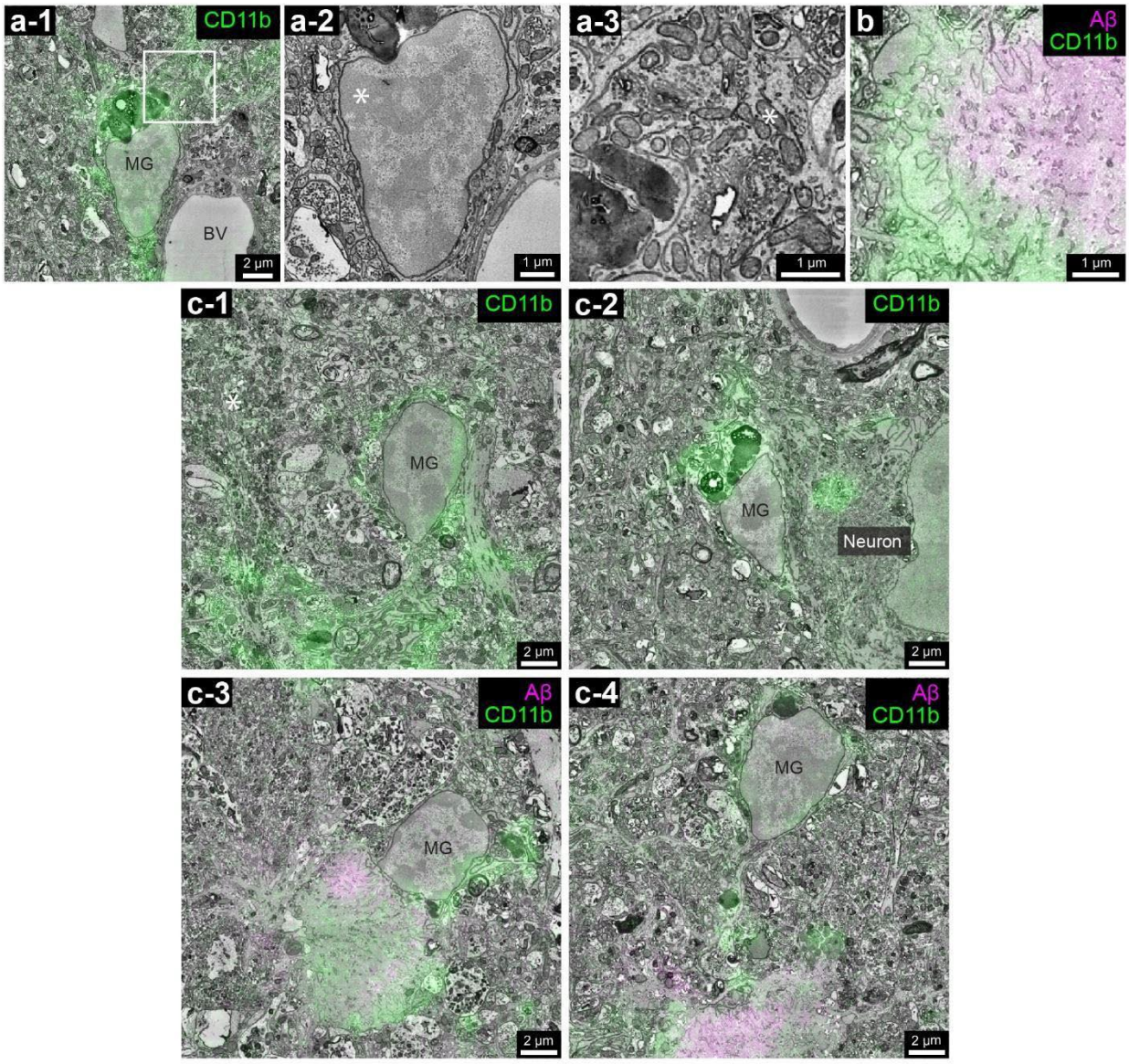

466

467 **Figure 8. Ultrastructural abnormalities that colocalize with the labeling of CD11b.**

468 **a-1**, green fluorescence from the anti-CD11b nanobody overlaps with a microglial cell. **a-2**, the nucleus of
469 the microglial cell in **a-1**. Asterisk indicates the condensed nucleoplasm. **a-3**, enlarged inset from **a-1**.
470 Asterisk indicates the altered mitochondria. **b**, green fluorescence from the anti-CD11b nanobody
471 overlaps with the glial processes encircling plaque material, which shows overlapped magenta
472 fluorescence from the anti-Aβ nanobody. **c-1**, green fluorescence from the anti-CD11b nanobody
473 overlaps with a microglial cell nearby dystrophic neurites (asterisks). **c-2**, green fluorescence from the
474 anti-CD11b nanobody overlaps with a microglial cell next to a pyramidal neuron (the same neuron in
475 Figure 6 c-1). **c-3** and **c-4**, green fluorescence from the anti-CD11b nanobody overlaps with two

476 microglial cells nearby plaque material, which shows overlapped magenta fluorescence from the anti-Aβ
477 nanobody.
478
479 **3D Reconstructions Reveal Detailed Morphological Features of Neurons with Intraneuronal Aβ or**
480 **pTau**

481 As a proof-of-principle demonstration of the dataset's potential, we conducted 3D reconstructions
482 of neurons with intraneuronal Aβ or pTau, showcasing the dataset's ability to uncover detailed,
483 unreported morphological features associated with these pathologies. Using the automatic segmentation
484 followed by manual proofreading, a pyramidal neuron with intraneuronal Aβ (Figure 7 c-1) and two
485 pyramidal neurons with intraneuronal pTau (Figure 6 b-1, c-1) were reconstructed.

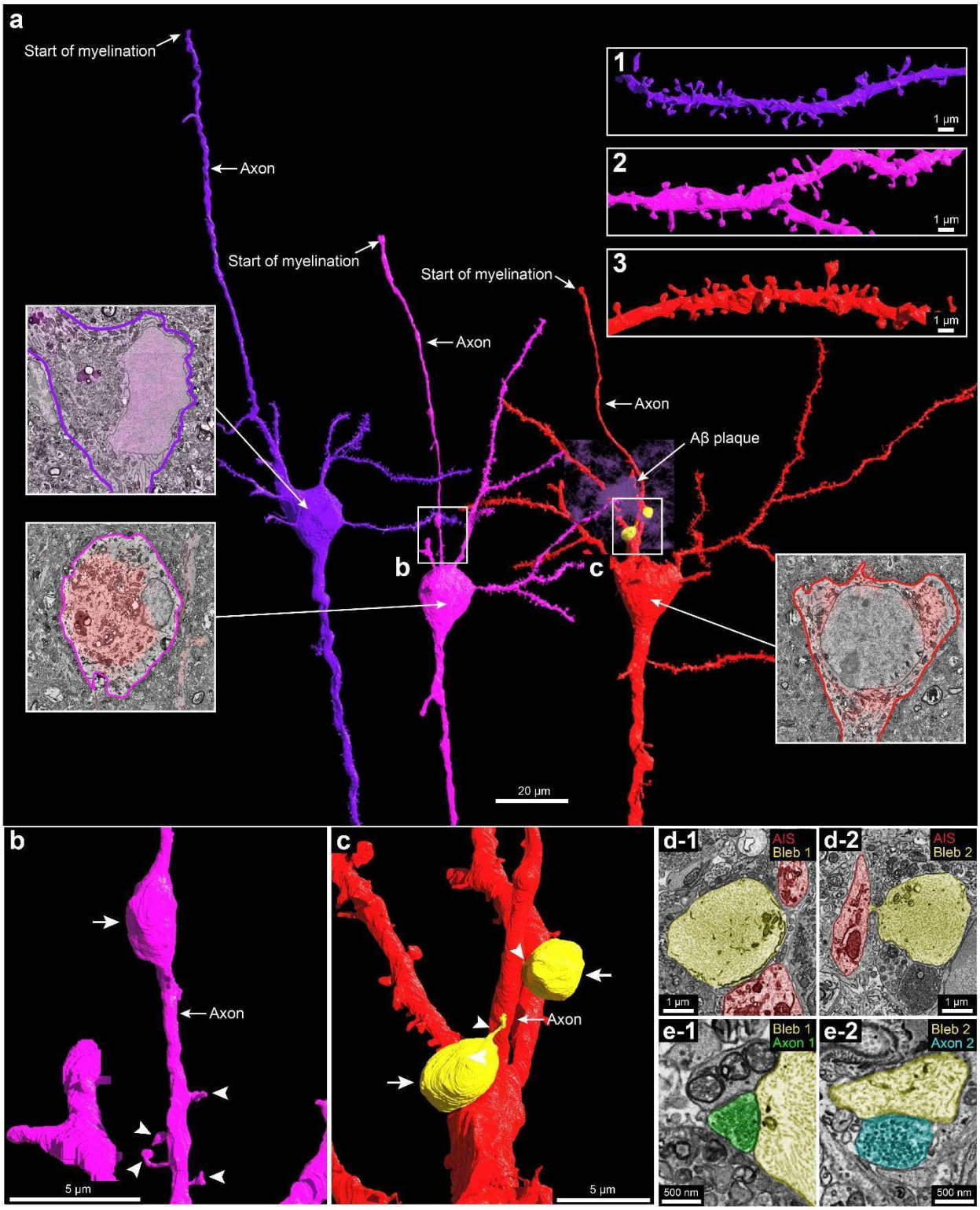

Figure 9. 3D reconstruction of a neuron with intracellular Aβ and two neurons with intracellular pTau.

a, 3D reconstruction of three pyramidal neurons. The insets pointing to the cell bodies show the labeling

490 of Aβ or pTau by nanobody probes. Insets 1 to 3 show segments of spiny dendrites of Neuron 1 to 3. **b**
491 shows the AIS of Neuron 2 as labeled in **a**. White arrow, the swelling filled with pTau. White arrow heads,
492 spines on AIS. **c** shows the AIS of Neuron 3 as labeled in **a**. White arrows, two pTau positive blebs
493 connected to the AIS. White arrows, thin stalks connecting the blebs to the AIS. **d-1** and **d-2**, 2D
494 segmentations of the two pTau positive blebs filled with straight filaments. **e-1** and **e-2** show that each of
495 the blebs was adjacent to an axon profile filled with synaptic vesicles.
496
497 The cell body of neuron 1 with intraneuronal Aβ labeling appeared abnormal as if it were in the
498 process of degenerating (Figure 7 c-1, c-2). A microglial cell was immediately adjacent raising the
499 possibility that the neuron would soon be phagocytosed (Figure 8 c-2). Surprisingly, this neuron still
500 retained multiple spiny dendrites (Figure 9 a, inset 1) and its axon projected normally for ~100 μm without
501 myelin and then showed normal myelination (Figure 9 a). Neuron 2 showed intraneuronal pTau labeling in
502 its soma (Figure 6 b-1, b-2). Nonetheless it also had multiple normal looking spiny dendrites (Figure 9 a,
503 inset 2). This neuron's axon ran normally ~80 μm before becoming myelinated (Figure 9 a). As was the
504 case for the other two neurons, there were several spine-like structures innervated by vesicle-filled axonal
505 profiles (Figure 9 b) along this neuron's axon initial segment (AIS). This AIS also had an abnormally
506 enlarged swelling that was positive for anti-pTau nanobody labeling. This swelling was filled with
507 lipofuscin granules (see Figure 6 h-1, h-2). The third neuron (Neuron 3) with intraneuronal pTau labeling
508 (Figure 6 c-1, c-2) was located such that its soma was adjacent to an Aβ plaque (Figure 9 a). This neuron
509 also possessed multiple normal looking spiny dendrites (Figure 9 a inset 3) and an axon with normal
510 appearance that ran ~60 μm before becoming myelinated (Figure 9 a). Two spine-like swollen
511 protrusions emerged from its AIS via narrow stalks (Figure 9 a box c, d-1, d-2; Figure 9 c). Each of these
512 was filled with straight filaments, similar to those described above (Figure 9 d-1, d-2; also see Figure 6 g-
513 1, g-2 and Sup. Figure 7 b). We suspect that these objects are abnormally enlarged postsynaptic spine
514 heads because they were innervated by vesicle-filled axonal profiles (Figure 9 e-1, e-2). The protrusion
515 stalks are extremely thin (less than 1 μm in diameter), suggesting the possibility that these structures may
516 eventually detach from the AIS. Supporting this hypothesis, we identified a nearby pTau-filled bleb that
517 appeared disconnected from the AIS or any adjacent structures (Sup. Figure 8).

518 **Analysis of synapse nearby an Aβ plaque reveals alterations in synapse density and size**

519 As another proof-of-principle demonstration of the robustness and utility of our dataset, we
520 applied the synapse prediction by supervised learning that has high precision and recall to investigate

synaptic alterations in proximity to an Aβ plaque—an area of critical interest given the central role of synaptic pathology in the etiology, manifestation, and progression of AD (Tzioras et al. 2023; Koffie, Hyman, and Spires-Jones 2011). We randomly selected nine 6 x 6 x 6 µm regions predominantly comprising neuropil. These regions included three representative areas located at distances of 10 µm, 20 µm, and 30 µm from the plaque center (Sup. Figure 9).

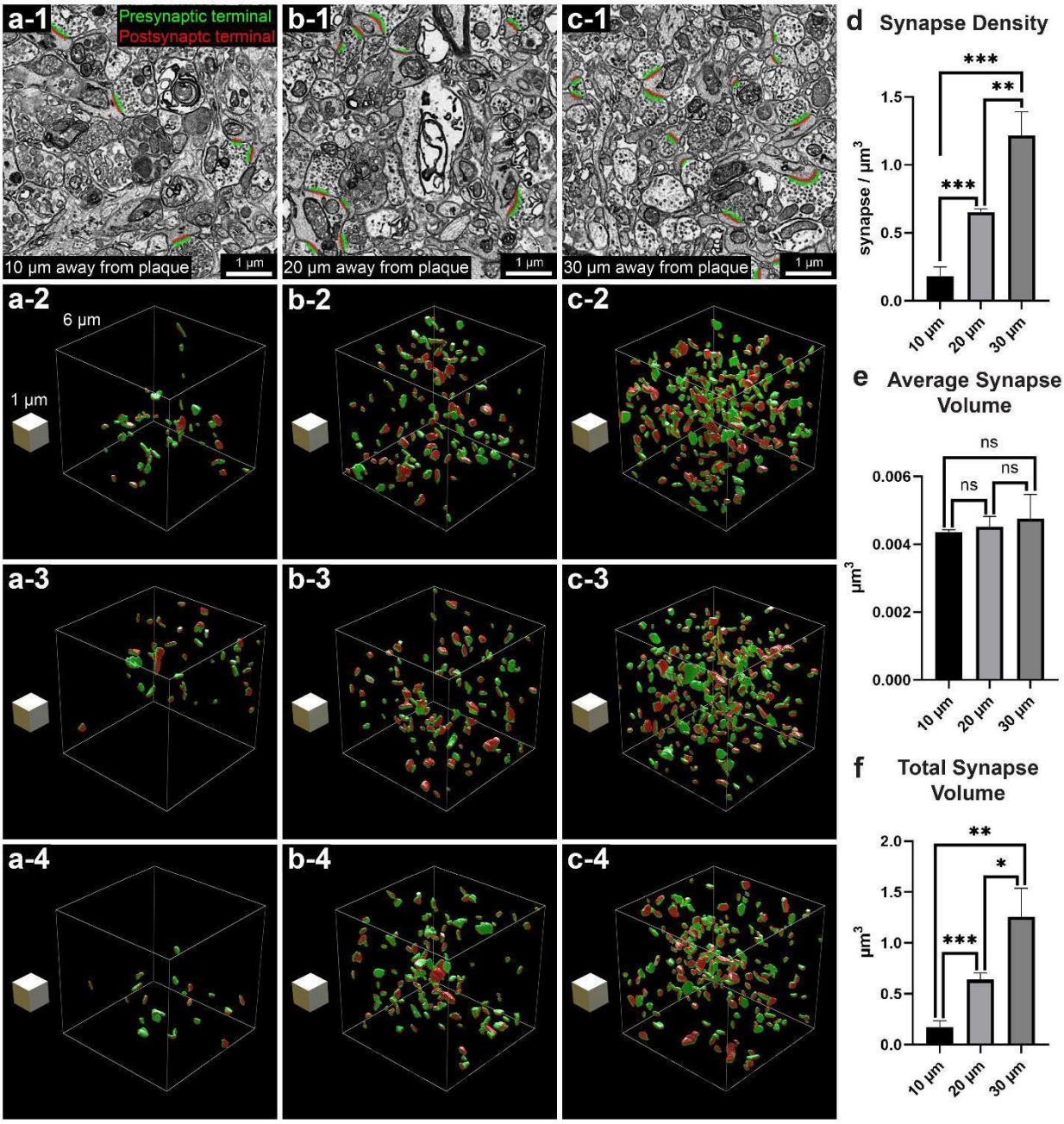

Figure 10. Changes in synapse density and total synapse volume with relationship to the distance from an extracellular Aβ plaque.

a-1, A representative image slice with detected synapses from the box at 10 μm away from the center of an Aβ plaque. **a-2** to **a-4**, 3D rendering of all detected synapses in the box as in **a-1** with the dimensions of 6 μm x 6 μm x 6 μm at 10 μm away from the center of an Aβ plaque. White block is of the dimension of 1 μm x 1 μm x 1 μm. **b-1**, A representative image slice with detected synapses from the box at 20 μm away from the center of an Aβ plaque. The image slice is of the dimension of 6 μm x 6 μm. **b-2** to **b-4**, 3D rendering of all detected synapses in the box as in **b-1** with the dimensions of 6 μm x 6 μm x 6 μm at 20 μm away from the center of an Aβ plaque. White block is of the dimension of 1 μm x 1 μm x 1 μm. **c-1**, A representative image slice with detected synapses from the box at 30 μm away from the center of an Aβ plaque. The image slice is of the dimension of 6 μm x 6 μm. **c-2** to **c-4**, 3D rendering of all detected synapses in the box as in **c-1** with the dimensions of 6 μm x 6 μm x 6 μm at 30 μm away from the center of an Aβ plaque. White block is of the dimension of 1 μm x 1 μm x 1 μm. **d**, Synapse density, **e**, Average synapse volume, **f**, Total synapse volume were measured for each of the three box at 10 μm away from the plaque, the three box at 20 μm away from the plaque, and the three box at 30 μm away from the plaque. Two-tailed, unpaired t-test was performed. Synapse density, 10 μm vs. 20 μm, $p = 0.0004$, $t=11.29$, $df=4$; 20 μm vs. 30 μm, $p = 0.0051$, $t=5.553$, $df=4$; 10 μm vs. 30 μm, $p = 0.0007$, $t=9.597$, $df=4$. Average synapse volume, 10 μm vs. 20 μm, $p = 0.4356$, $t=0.8655$, $df=4$; 20 μm vs. 30 μm, $p = 0.6104$, $t=0.5519$, $df=4$; 10 μm vs. 30 μm, $p = 0.3864$, $t=0.9713$, $df=4$. Total synapse volume, 10 μm vs. 20 μm, 0.0009, $t=8.789$, $df=4$; 20 μm vs. 30 μm, $p = 0.0210$, $t=3.690$, $df=4$; 10 μm vs. 30 μm, $p = 0.0029$, $t=6.489$, $df=4$.

Synapse detection on all nine boxes (Figure 10 a-1 to a-3, b-1 to b-3, c-1 to c-3) showed that a decrease in synapse density as regions progressively closer to the plaque: synapse density was 0.181 ± 0.068 per μm³ at 10 μm, 0.653 ± 0.025 per μm³ at 20 μm, 1.216 ± 0.174 per μm³ at 30 μm (Figure 10 d). There was a statistically significant trend as the distance to the plaques dropped from 30 μm to 10 μm (two-tailed, unpaired t-test. 10 μm vs. 20 μm, $p = 0.0004$; 20 μm vs. 30 μm, $p = 0.0051$; 10 μm vs. 30 μm, $p = 0.0007$).

The average synapse volume (pre-synaptic side) was 0.00436 ± 0.00007 μm³ at 10 μm, 0.00452 ± 0.00030 μm³ at 20 μm, 0.00476 ± 0.00071 μm³ at 30 μm (Figure 10 e). There was no statistically significant change in average synapse volume as the distance to the plaques dropped from 30 μm to 10 μm (two-tailed, unpaired t-test. 10 μm vs. 20 μm, $p = 0.4356$; 20 μm vs. 30 μm, $p = 0.6104$; 10 μm vs. 30 μm, $p = 0.3864$).

The total synaptic volume (pre-synaptic side) for each was 0.170 ± 0.065 μm³ at 10 μm, 0.638 ± 0.066 μm³ at 20 μm, 1.255 ± 0.282 μm³ at 30 μm (Figure 10 f). There was a statistically significant decrease in total synaptic volume as the distance to the plaques dropped from 30 μm to 10 μm (two-tailed, unpaired t-test. 10 μm vs. 20 μm, $p = 0.0009$; 20 μm vs. 30 μm, $p = 0.0210$; 10 μm vs. 30 μm, $p = 0.0029$).

To investigate whether smaller synapses are more susceptible to elimination, suggested by previous studies (John and Reddy 2021; Meftah and Gan 2023)—we combined synapse volume data

567 (pre-synaptic + post-synaptic) from the three boxes at each distance and analyzed the frequency
568 distributions (Sup. Figure 10). We performed two-sample Kolmogorov–Smirnov tests and found there was
569 no significant difference between any two of the distributions (10 μm vs. 20 μm: $p = 0.8498$; 20 μm vs. 30
570 μm: $p = 0.1231$; 10 μm vs. 30 μm: $p = 0.09247$). This result suggests that there was synapse elimination
571 closer to the plaque, but the elimination did not preferentially target smaller nor larger synapses.
572 Synapses of all volumes were possibly eliminated equally when closer to the plaque. To further test
573 whether one of the pre-synaptic site or post-synaptic is affected more, we plotted the frequency
574 distributions of pre- or post-synaptic volumes (pre-synaptic, Sup. Figure 11 a; post-synaptic, Sup. Figure
575 11 b) for all nine boxes. We found that the pre-synaptic volumes of all boxes were slightly larger than the
576 post-synaptic volumes (Sup. Figure 11 c).
577

578 **Conclusions and Discussion**

579 This work introduces a volumetric correlated light and electron microscopy (vCLEM) technique
580 using fluorescent nanobody immunolabeling to localize Alzheimer's disease (AD)-related molecules,
581 including phosphorylated tau (pTau), amyloid-β (Aβ), and CD11b, in a large-scale volume EM dataset
582 from an AD mouse model. By preserving ultrastructure through detergent-free labeling, this method
583 addresses a major limitation of conventional volume EM-based connectomics, which lacks molecular
584 specificity, and overcomes the challenges posed by traditional molecular labeling techniques that often
585 compromise sample integrity. The resulting dataset enables precise localization of pathological proteins
586 within their ultrastructural context, allowing for integrated analyses at molecular, cellular, and circuit levels
587 across a significantly larger volume than previous vEM datasets.

588 The publicly accessible dataset, featuring advanced machine-learning-based segmentations of
589 neurons, dendrites, axons, glial processes, and synapses, offers a valuable resource for studying AD
590 pathology. Researchers can pinpoint cellular and subcellular structures where Aβ and pTau localize,
591 reconstruct affected cells at nanometer resolution, and investigate how these pathological markers impact
592 synaptic connectivity and neuronal networks. This dataset lowers the entry barrier for researchers less
593 familiar with volume EM or segmentation tools, fostering broader participation in connectomics-driven AD
594 research.

595 Following the above framework, as a proof-of-principle, we used our dataset to identify novel
596 pTau-associated abnormalities at the axon initial segment (AIS), including enlarged blebs filled with
597 straight filaments and pTau-positive swellings containing lipofuscin granules (Figure 6 g-1, g-2). These
598 findings highlight the complex landscape of pTau pathology, where certain aggregates lack visible
599 neurofibrillary tangle-like features in EM micrographs. We also observed spine-like structures at the AIS
600 with thin stalks (Figure 9 c; less than 1 μm in diameter), potentially prone to detachment, raising the
601 intriguing hypothesis that these structures may contribute to exosome formation, a mechanism implicated
602 in pTau release in AD (Saman et al. 2012; Miyoshi et al. 2021). These abnormalities suggest disrupted
603 molecular mechanisms at the AIS, likely involving ankyrin-G (Sobotzik et al. 2009; Zempel et al. 2017) or
604 diffusion barriers affected by pTau or Aβ (X. Li et al. 2011), leading to tau missorting and synaptic
605 dysfunction (Blazquez-Llorca et al. 2011). The AIS's established role as a barrier for regulating tau
606 trafficking underscores the potential of these disruptions to impact synaptic transmission significantly. For
607 Aβ, in addition to extracellular deposits in plaques, we identified neurons with intraneuronal Aβ deposits
608 exhibiting severe morphological abnormalities, including tortuous dendrites, shrunken cell bodies, and
609 degenerating organelles. These features indicate profound cellular dysfunction and are consistent with
610 Aβ's known neurotoxicity. Interestingly, 3D reconstructions enabled by machine-learning segmentation
611 provided a detailed view of these affected neurons and revealed novel morphologies not easily captured
612 by prior FIB-SEM and ATUM-SEM datasets, which were limited to smaller subvolumes (Montero-Crespo
613 et al. 2021; Domínguez-Álvaro et al. 2018; Jiang et al. 2022; Pang et al. 2022; Blazquez-Llorca et al.
614 2013).
615 Our synapse analysis further revealed significant alterations near Aβ plaques. Synapse density
616 declined sharply with proximity to plaques, reflecting Aβ's synaptotoxic effects (Hampel et al. 2021; Koffie
617 et al. 2009; Urbanc et al. 2002) and glial-mediated mechanisms (Chung et al. 2015; Rajendran and
618 Paolicelli 2018; Vilalta and Brown 2018). Reactive glial processes from microglia and astrocytes were
619 notably abundant near plaques (Figure 8 b, also see Sup. Figure 11 for astrocytic processes), supporting
620 their role in synaptic pruning and dysfunction. While synapse density decreased, the average synapse
621 volume remained constant, resulting in a reduction in total synapse volume near plaques. This challenges
622 earlier findings suggesting compensatory synaptic enlargement with declining synapse density (Scheff

623 and Price 2001; Neuman et al. 2015; Androuin et al. 2018; Scheff and Price 2003). Instead, our results
624 align with more recent volume EM studies showing no evidence of synaptic enlargement (Martínez-Serra
625 et al. 2022). Future classification of synapses by type (e.g., excitatory vs. inhibitory) or location (e.g.,
626 somatic vs. dendritic) could clarify whether specific subpopulations respond differently to Aβ toxicity.
627 While the vCLEM approach provides transformative insights, it has limitations. We focused on
628 two canonical markers—fibrillar Aβ40/42 and pTau phosphorylated at specific sites—without addressing
629 other molecular forms known to elicit more severe toxicity. Additionally, the limited availability of
630 nanobody probes constrains the range of molecules that can be studied. The resolution gap between
631 confocal fluorescence microscopy and EM may introduce slight inaccuracies in registering molecular
632 signals onto EM micrographs. Furthermore, findings from this single-sample study require validation in
633 additional datasets, including other animal models and human tissues, to ensure broader applicability.
634 A key future direction involves expanding the repertoire of fluorescent nanobody probes to target
635 a broader range of pathological molecules. For instance, probes could be developed for specific Aβ
636 species (e.g., Aβ1-40 and Aβ1-42) and conformations (e.g., oligomers, protofibrils, and fibrils) (Hampel et
637 al. 2021), as well as tau isoforms or site-specific phosphorylations (Arendt, Stieler, and Holzer 2016).
638 These advancements would enable more detailed analyses of molecular variants with distinct toxicities
639 affecting neurons and synapses. Furthermore, nanobody probes for other neurodegeneration-related
640 molecules, such as α-synuclein (Twohig and Nielsen 2019), TDP-43 (transactive response DNA-binding
641 protein of 42 kDa) (Wilson et al. 2011), PLD3 (Nackenoff et al. 2021; Hooli et al. 2015), and SORL1
642 (sortilin-related receptor 1), which plays a crucial role in neuronal endosome trafficking (Yin, Yu, and Tan
643 2015; Knupp et al. 2020), as well as huntingtin (Bates et al. 2015), could significantly broaden the utility of
644 this technique. These additions would expand its application beyond Alzheimer's disease to other forms
645 of dementia and neurodegenerative disorders. Many nanobodies for these targets already exist (Danis et
646 al. 2022; De Genst et al. 2010; Habicht et al. 2007; Lafaye et al. 2009) and could be easily adapted into
647 fluorescent probes. Beyond pathological proteins, this approach can also be extended to cell-type-specific
648 markers, allowing researchers to investigate how toxic molecules impact distinct cell populations. For
649 example, nanobody or single-chain variable fragment (scFv)-based probes could target markers for glial
650 cells or inhibitory neuron subtypes, providing insights into cell-type-specific vulnerabilities and

651 mechanisms in Alzheimer's disease and other neurodegenerative conditions.

652 Recent large-scale proteomic and transcriptomic studies (Johnson et al. 2022, 2020; Magistri et
653 al. 2015; Mathys et al. 2019) have showed alterations at the levels of protein and gene expression in AD.
654 To localize these new molecular abnormalities in connectomics datasets, a large collection of nanobody
655 probes that target common molecular markers will be needed. Multiple nanobody databases are now
656 available where thousands of nanobody sequences are being deposited (Deszyński et al. 2021; Wilton et
657 al. 2018). Researchers can query sequences of nanobodies that target the molecular abnormalities of
658 interest, and then, as we have done, convert these nanobodies into fluorescent probes. If no nanobody
659 for a desired target is available, there are efficient ways to generate new nanobodies from immune
660 libraries (Muyldermans 2021) or synthetic libraries (McMahon et al., 2018; Zimmermann et al.,
661 2020)(McMahon et al. 2018; Zimmermann et al. 2020).

662 With a growing collection of nanobody probes, integrating vCLEM with super-resolution
663 microscopy (Hoffman et al., n.d.; Tuijtel et al. 2019) could enhance the precision of molecular target
664 localization within EM micrographs. Combining vCLEM with advanced multiplex imaging techniques, such
665 as super-multicolor fluorescence imaging enabled by spectral unmixing (Seo et al. 2022) or multiplexed
666 Raman vibrational imaging (Wei et al. 2017), could allow for the simultaneous labeling of numerous
667 markers in a single sample. This would unlock unprecedented opportunities for integrative molecular and
668 structural studies, enabling a deeper understanding of complex pathological processes.

669 Notably, this technique is well-suited for application to human samples, as it does not rely on
670 transgenic models and can directly target molecules in human tissues using nanobody probes. The
671 nanobody probes tested in this study (A2 and R3VQ) have already been shown to effectively detect their
672 targets in brain samples from AD patients (T. Li et al. 2016). By integrating this approach with recently
673 developed methods for processing large surgical brain samples (Karlupia et al. 2023; Loomba et al.
674 2022), vCLEM offers a powerful tool for investigating AD connectomics directly in human tissues,
675 providing critical insights into disease mechanisms and pathology.

676 This study highlights the transformative potential of vCLEM for bridging molecular and structural
677 data in large-scale volume EM datasets, offering a publicly accessible resource to advance integrative
678 research into AD and other neurodegenerative diseases.

679

680 ## Material and Methods

681 ### Animals

682 Animals used in the study were female one-year old 3xTg (B6;129-Tg(APPSwe,tauP301L)1Lfa
683 Psen1$^{tm1Mpm/Mmjax}$) mice (Jackson Laboratory) and female one-year old B6129SF2/J mice (as age-
684 matched control animal, Jackson Laboratory). All experiments using animals were conducted according
685 to US National Institutes of Health guidelines and approved by the Committee on Animal Care at Harvard
686 University.

687 ### Nanobody immuno-probe production

688 A signal peptide (MDWTWRILFLVAAATGAHS) was added to the N'-terminus of the nanobody. A
689 sortase tag (SLPETGG) and a 6 x His tag was added to the C'-terminus. The amino acid sequence was
690 reverse translated into a DNA sequence with codon optimization for human cells. The DNA sequence
691 was synthesized and cloned into pcDNA 3.1 vectors.

692 Nanobody expression was performed with Expi 293 cells (ThermoFisher). Detailed expression,
693 purification, and dye conjugation protocols can be found in Sup. File.

694 ### Perfusion and fixation

695 The mouse was anesthetized by isoflurane until there was no toe-pinch reflex. Mice were then
696 transcardially perfused with aCSF (125 mM NaCl, 26 mM $NaHCO_3$, 1.25 mM NaH_2PO_4, 2.5 mM KCl, 26
697 mM glucose, 1 mM $MgCl_2$ and 2 mM $CaCl_2$ (all chemicals from Sigma-Aldrich) at the flow rate of 10
698 ml/min for 2 min to remove blood, followed with 4% paraformaldehyde (Electron Microscopy Sciences),
699 0.1% glutaraldehyde (Electron Microscopy Sciences) in 1 x PBS for 3 min for fixation. Brains were
700 dissected and then post-fixed in the same fixative on a rotator overnight at 4°C. Brains were sectioned
701 into 50-μm or 120-μm coronal sections using a Leica VT1000 S vibratome and stored in the same fixative
702 at 4°C.

703 ### Immunofluorescence

704 Detergent-free immunofluorescence labeling was performed with nanobody probes (see Sup.
705 Table 1 for the nanobody probes and the final concentration of each nanobody probe used in this study).

706 The detailed protocol was described in (Han et al. 2024). For the 120-μm coronal sections used for
707 vCLEM, the section was first washed with 1 x PBS for 3 x 10 min, and then blocked in glycine blocking
708 buffer (0.1 M glycine, 0.05% NaN_3 in 1 x PBS) for 1 h on a rotator at 4 °C. The labeling solution was
709 prepared by diluting nanobody-dye conjugates in glycine blocking buffer (see Sup. Table 1 for the final
710 concentration used). The labeling solution and any remaining steps were protected from light. The section
711 was incubated with the labeling solution on a rotator at 4 °C for three to seven days. The 120-μm sections
712 for Figure 2 were first incubated with the labeling solution with only the anti-pTau nanobody for three
713 days, and then incubated with the labeling solution with the anti-Aβ and the anti-CD11b nanobodies for
714 another three days. The 120-μm section for Figure 3 was incubated with the labeling solution with all four
715 nanobodies for seven days. After the incubation, the section was washed with 1 x PBS for 3 x 10 min,
716 and then stained with Hoechst 33342 (Invitrogen, diluted 1:5000 in 1 x PBS) for 1 h on a rotator at 4 °C.
717 The section was washed with 1 x PBS for 3 x 10 min, and then mounted onto glass slide (VWR).
718 To validate the labeling of the nanobody A2, double immunofluorescence labeling with detergent
719 was performed on 50-μm sections with the anti-pTau mAb AT8 (ThermoFisher) plus the anti-mouse IgG
720 H + L secondary antibody conjugated with Alexa Fluor 488 (ThermoFisher), and A2 conjugated with Alexa
721 Fluor 594 (see Sup. Figure 1 a) (see Sup. Table 2 and 3 for the final concentrations used for each probe).
722 To validate the labeling of the nanobody R3VQ, double immunofluorescence labeling with detergent was
723 performed with the anti-Aβ mAb 4G8 conjugated with Alexa Fluor 647 (BioLegend) and R3VQ conjugated
724 with 5-TAMRA (see Sup. Figure 2) (see Sup. Table 2 and 3 for the final concentrations used for each
725 probe). The detailed protocol is available on the NeuroMab website ("Welcome to NeuroMab!," n.d.). In
726 brief, 50-μm coronal sections were first washed with 1 x PBS for 3 x 10 min, and then blocked in vehicle
727 (10% normal goat serum, 0.3% Triton X-100 in 1 x PBS) overnight on a rotator at 4 °C. Subsequent steps
728 were protected from light. For the experiment with AT8 and A2, the sections were then incubated with
729 primary antibody solution plus nanobody probes overnight on a rotator at 4 °C. After the incubation,
730 sections were washed with vehicle for 3 x 10 min, and then incubated with the secondary antibody
731 solution for 1 hour on a rotator at 4 °C. For the experiment with 4G8 and R3VQ, the sections were then
732 incubated with primary antibody solution plus nanobody probes for 3 days on a rotator at 4 °C. After the
733 incubation, sections were washed with 1 x PBS for 3 x 10 min, and then stained with Hoechst (diluted

734 1:5000 in 1 x PBS) for 1 h on a rotator at 4 °C. Sections were washed with 1 x PBS for 3 x 10 min, and
735 then mounted onto glass slides.

736 **Fluorescence confocal microscopy**

737 Fluorescence confocal microscopy was performed as described in (Han et al. 2024). In brief, 50-
738 µm sections were mounted in Vectashield H-1000 (Vector Laboratories) with a #1 coverslip (Electron
739 Microscopy Sciences) on top sealed with clear nail polish. 120-µm sections (for vCLEM) were mounted in
740 1 x PBS inside 120-um spacer (Invitrogen) with a #1 coverslip on top sealed with the spacer. Sections
741 were imaged with a Zeiss LSM 880 confocal laser scanning microscope equipped with either a 20x/0.8
742 NA air-objective or a 40x/1.1 NA water immersion objective. The 120-µm section for vCLEM was imaged
743 with a 40x/1.1 NA water immersion objective. Acquisition of double or triple color fluorescent images was
744 done with appropriate band pass filters for the specific fluorescent dyes to avoid crosstalk.

745 The brightness, contrast, and gamma of all fluorescent images were adjusted. Fluorescence
746 image volumes were projected to a single plane by maximum intensity for visualization in 2D.

747 **EM preparation**

748 Sample preparation for electron microscopy was performed as described in (Han et al. 2024).
749 After the 120-µm sections was imaged, it was transferred into 3.7 ml shell vials with 1 ml secondary
750 fixative (2% PFA, 2,5% glutaraldehyde in 0.15M sodium cacodylate buffer with 4mM Ca^{2+} and 0.4 mM
751 Mg^{2+}) and incubated for at least one week on a rotator at 4 °C. A modified ROTO (Reduced Osmium-
752 Thiocarbohydrazide-Osmium) protocol was used to stain the section. The section was embedded in LX-
753 112 resin.

754 **X-ray microCT scanning**

755 X-ray micro-computed tomography (µCT) images of the resin-embedded sections were acquired
756 using a Zeiss Xradia 510 Versa system and Zeiss' Scout and Scan software. Detailed protocol was
757 described in (Han et al. 2024).

758 **EM imaging**

759 The resin-embedded sections were cut into 30 nm serial ultrathin sections using automated tape-
760 collecting ultramicrotome (ATUM) (Kasthuri et al. 2015). Serial sections were collected onto carbon-

761 coated and plasma-treated Kapton tape. The tape was cut into strips and affixed onto 150 mm silicon
762 wafers (University Wafer). A Zeiss Sigma scanning electron microscope was used to acquire overview
763 images from the serial sections. Detailed protocol was described in (Han et al. 2024).

764 Prior to acquiring high-resolution images, the serial section sections on wafers were post-stained
765 for 4 min with a 3% lead citrate solution. After staining, the sections were degassed for a minimum of 24 h
766 at 1x10-6 Torr. A Zeiss MultiSEM 505 scanning electron microscope equipped with 61 electron beams
767 was used to acquire high-resolution images from the serial sections. Images were collected using a 1.5-
768 kV landing energy, 4-nm image pixel, and a 400-ns dwell time.

769 **High-resolution EM image processing**

770 The preparation of the vEM data before it could be segmented/analyzed includes two steps:
771 affine stitching and elastic alignment. Detailed protocol was described in (Han et al. 2024). We excluded
772 20 slices that had sub-optimal imaging quality (e.g. very thin slices or contains tears and wrinkles) and
773 copied the adjacent sections in the places of these excluded slices. The aligned stack was rendered at
774 full resolution (4 x 4 x 30 nm) and each section was cut into 4k x 4k .png tiles, imported into VAST as a
775 .vsvi file, and ingested into Neuroglancer for further analysis.

776 The initial alignment of the vEM dataset showed several jumps through the z-axis. A second
777 attempt at alignment was performed after discarding four more slices (we also copied the adjacent
778 sections in the places of these discarded slices) that had suboptimal image quality, which successfully
779 eliminated the jumps. The 3D reconstruction of Neuron 3, the automatic Aβ plaque detection, and the
780 synapse detection using a U-Net classifier was performed on the first version of alignment. The 3D
781 reconstruction of Neuron 3 and the automatic Aβ plaque detection were later transferred to the second
782 version of the alignment based on matching coordinates. The other reconstructions and the synapse
783 detection by PyTorch were performed on the second version of the alignment. The publicly accessible
784 vCLEM dataset shows the second version of the alignment.

785 **Co-registration of fluorescence and EM volumes**

786 The co-registration was performed using the BigWarp plugin in FIJI. Detailed description can be
787 found in (Han et al. 2024).

Automatic segmentation

We segmented a central cutout of the dataset using flood-filling networks (Michał Januszewski et al. 2018). The FFN segmentation model was trained at 16 x 16 x 33 nm nominal resolution on the H01 dataset (Shapson-Coe et al. 2024), and run here on CLAHE intensity normalized data (Zuiderveld 1994) downsampled to 16 x 16 x 30 nm. Direct application of the H01-trained FFN to the AD dataset did not perform well, particularly on thinner objects. Therefore we used Segmentation Enhanced CycleGANs (Michal Januszewski and Jain 2019) to modify the visual appearance (photometrics, noise statistics, staining, etc.) of the AD dataset at 16 x 16 x 30 nm to mimic H01, prior to running the FFN. We trained the SECGAN style transfer on a central cutout of the AD dataset totaling 240 x 160 x 15 um and a cutout of H01 totaling 1600 x 760 x 130 um for 8 million steps at batch size 1. The SECGAN generator architecture was an 8-layer fully convolutional stack with residual connections and no downsampling, and the discriminator was a ResNet18 (He et al., n.d.).

2D membrane detection at 4 x 4 x 30 nm resolution was performed on the vEM dataset using a method developed in our lab. A description of this approach was given in (Karlupia et al. 2023; Meirovitch et al. 2018; Pavarino et al. 2023). In brief, an algorithm (Pavarino et al. 2023) pre-trained on a mouse cerebellar dataset was used to generate 2D membrane detection. 2D membrane detection was use for filtering false positive in synapse prediction.

Synapse detection by supervised leaning

We sampled nine EM image subvolumes with dimensions of 6 μm x 6 μm x 6 μm at three distances (10 μm, 20 μm, 30 μm) from the center of an Aβ plaque at the original resolution. We took a semi-automatic approach to annotate all the synapses in these subvolumes. First, one human annotator labeled all the pre- and post-synaptic appositions in 1/4 of one of the nine EM image subvolumes. Then, we trained a synapse detection model (Parag et al. 2019) using the manual annotations with the PyTorch Connectomics deep learning package. To refine the model, we tested it on all slices of this subvolume, manually proofread its results, and fine-tuned the model with all the annotations, which led to a desirable detection accuracy and recall result. Lastly, we used the improved model to detect synapses in the entire dataset and identified 3.5 million synapses..

815 **Synapse detection by transfer learning**

816 The original synapse annotation model was a UNet (3-down and 3-up modules) trained at 8 x 8 x
817 33 nm nominal resolution on the H01 dataset (Shapson-Coe et al. 2024). For the initial synapse
818 predictions, we used the SECGAN model trained for 683k steps to style-transfer an ROI of the AD data to
819 mimic H01, and then ran a synapse model that was trained for 786k steps on H01. This produced 0.255
820 million synapse masks, with low rates of precision and recall. We then used the model-inferred synapse
821 masks as automated ground truth to train a new UNet from scratch directly on the AD data (8 x 8 x 30 nm
822 resolution, without SECGAN style transfer, but with CLAHE). We trained this model for 38M steps and
823 biased it against false negatives by weighting positively labeled pre- and post-synaptic voxels in the
824 training data by 2x. The new synapse annotation model produced 2.1 million raw synapse masks, which
825 resulted in 0.732 million total synapses after filtering for synapses above a 100 voxel volume threshold,
826 removing any pairs that had identical pre- and post-synaptic parents (i.e. self-synapses) and masking out
827 synaptic sites residing on blood vessels, somas, or myelin. We estimated the final precision and recall as
828 46% and 52% based on evaluation against the manualy annotated subvolume in the first method of
829 synapse detection.

830 **Automatic Aβ plaque segmentation**

831 We optimized a DeepLab-v3 semantic segmentation model (L.-C. Chen et al. 2018) on a cropped
832 stack of images with manually identified Aβ plaque. The model was pre-trained on another vEM dataset
833 from the Alzheimer's disease mouse model Tg2576 (Dr. Olga Morozova, personal communication) to
834 decrease the requirements of manually annotated training data in the target volume. We also oversample
835 patches near the Aβ plaque border during training to improve segmentation quality as the mask structures
836 in those patches are more challenging. The training and inference are implemented with the open-source
837 PyTorch Connectomics codebase.

838 **Statistical analysis**

839 Two-tailed, unpaired t-tests on synaptic density, synaptic volume and total synaptic volume of the
840 three categories defined in the section of synapse detection (The PyTorch method) were performed in
841 Prism-GraphPad. Two-sample Kolmogorov–Smirnov test was performed using Python.

842

Acknowledgement

We thank the Harvard Center for Biological Imaging (RRID:SCR_018673) for infrastructure and support, the Biopolymers and Proteomics Core Facility at the Koch Institute at MIT for processing the peptide-fluorescent dye conjugates, the Bauer Core Facility at Harvard for infrastructure and support, Dr. Olga Morozova for helpful discussion on the Alzheimer's disease mouse model and immunolabeling of Aβ plaques, and Dr. Marta Montero-Crespo for helpful discussion on synapse annotation. This work was supported by NIH grants U19 NS104653, UG3 MH123386, and P50 MH094271 (J. W. L.); NSF grants NSF-CAREER-2239688 (D. W.), NCS-FO-2124179, and NCS-FO-1835231 (H. Pfister.), NLM T15LM007092-31 (M. S.); Office of Naval Research grant N00014-20-1-2828 (J. W. L). X. H. was supported by the Edward R. and Anne G. Lefler predoctoral fellowship from the Lefler Center for Neurodegenerative Disorders at Harvard Medical School and the Simmons Awards from the Harvard Center for Biological Imaging.

Author Contribution

X. H. and J. W. L conceived this study. Nanobody A2 and R3VQ were originally generated in the labs of P. L., S. B., and B. D.. X. H. generated the fluorescent nanobody probes A2 and R3VQ. H. Ploegh provided the fluorescent anti-CD11b, anti-GFAP, and anti-Ly6C/6G nanobodies. X. H. performed the LM experiments. X. H. and R. S. performed the EM experiments. S. W. performed the imaging processing of the vEM dataset. P. H. L. and V. J. performed 3D segmentation and curated the vCLEM dataset at Neuroglancer. X. H., M. S., and F. A. performed 3D reconstruction of neurons. S. A., B. G., D. W., and X. H. performed synapse prediction through supervised learning.T. B. performed synapse detection through transfer learning. Y. M. (yaron.mr@gmail.com) performed 2D membrane detection. M. S. performed the filtering of the synapse detection results using a U-Net classifier. Z. L., and H. Pfister performed automatic plaque detection. D. B. provided the reconstruction tool VAST and advice on 3D reconstruction and rendering. Y. W. helped with LM and EM co-registration. X. H. and J. W. L wrote the paper with inputs from H. Ploegh, B. D., D. B., and R. S.

Competing interests

The authors declare no competing interests.

References

"2024 Alzheimer's Disease Facts and Figures." 2024. *Alzheimer's & Dementia: The Journal of the Alzheimer's Association* 20 (5): 3708–3821.

Androuin, Alexandre, Brigitte Potier, U. Valentin Nägerl, Daniel Cattaert, Lydia Danglot, Manon Thierry, Ihsen Youssef, et al. 2018. "Evidence for Altered Dendritic Spine Compartmentalization in Alzheimer's Disease and Functional Effects in a Mouse Model." *Acta Neuropathologica* 135 (6): 839–54.

Arendt, Thomas, Jens T. Stieler, and Max Holzer. 2016. "Tau and Tauopathies." *Brain Research Bulletin* 126 (Pt 3): 238–92.

Barbone, Giacomo E., Alberto Bravin, Alberto Mittone, Alexandra Pacureanu, Giada Mascio, Paola Di Pietro, Markus J. Kraiger, et al. 2022. "X-Ray Multiscale 3D Neuroimaging to Quantify Cellular Aging and Neurodegeneration Postmortem in a Model of Alzheimer's Disease." *European Journal of Nuclear Medicine and Molecular Imaging* 49 (13): 4338–57.

Barucker, Christian, Anja Harmeier, Joerg Weiske, Beatrix Fauler, Kai Frederik Albring, Stefan Prokop, Peter Hildebrand, et al. 2014. "Nuclear Translocation Uncovers the Amyloid Peptide Aβ42 as a Regulator of Gene Transcription." *The Journal of Biological Chemistry* 289 (29): 20182–91.

Bates, Gillian P., Ray Dorsey, James F. Gusella, Michael R. Hayden, Chris Kay, Blair R. Leavitt, Martha Nance, et al. 2015. "Huntington Disease." *Nature Reviews. Disease Primers* 1 (April):15005.

Belfiore, Ramona, Alexis Rodin, Eric Ferreira, Ramon Velazquez, Caterina Branca, Antonella Caccamo, and Salvatore Oddo. 2019. "Temporal and Regional Progression of Alzheimer's Disease-like Pathology in 3xTg-AD Mice." *Aging Cell* 18 (1): e12873.

Bisht, Kanchan, Kaushik P. Sharma, Cynthia Lecours, Maria Gabriela Sánchez, Hassan El Hajj, Giampaolo Milior, Adrián Olmos-Alonso, et al. 2016. "Dark Microglia: A New Phenotype Predominantly Associated with Pathological States." *Glia* 64 (5): 826–39.

Blazquez-Llorca, Lidia, Virginia Garcia-Marin, Paula Merino-Serrais, Jesús Ávila, and Javier DeFelipe. 2011. "Abnormal Tau Phosphorylation in the Thorny Excrescences of CA3 Hippocampal Neurons in Patients with Alzheimer's Disease." *Journal of Alzheimer's Disease: JAD* 26 (4): 683–98.

Blazquez-Llorca, Lidia, Ángel Merchán-Pérez, José-Rodrigo Rodríguez, Jorge Gascón, and Javier DeFelipe. 2013. "FIB/SEM Technology and Alzheimer's Disease: Three-Dimensional Analysis of Human Cortical Synapses." *Journal of Alzheimer's Disease: JAD* 34 (4): 995–1013.

Bogovic, John A., Philipp Hanslovsky, Allan Wong, and Stephan Saalfeld. 2016. "Robust Registration of Calcium Images by Learned Contrast Synthesis." In *2016 IEEE 13th International Symposium on Biomedical Imaging (ISBI)*, 1123–26.

Buhmann, Julia, Arlo Sheridan, Caroline Malin-Mayor, Philipp Schlegel, Stephan Gerhard, Tom

Kazimiers, Renate Krause, et al. 2021. “Automatic Detection of Synaptic Partners in a Whole-Brain Drosophila Electron Microscopy Data Set.” *Nature Methods* 18 (7): 771–74.

Chen, Guo-Fang, Ting-Hai Xu, Yan Yan, Yu-Ren Zhou, Yi Jiang, Karsten Melcher, and H. Eric Xu. 2017. “Amyloid Beta: Structure, Biology and Structure-Based Therapeutic Development.” *Acta Pharmacologica Sinica* 38 (9): 1205–35.

Chen, Liang-Chieh, Yukun Zhu, George Papandreou, Florian Schroff, and Hartwig Adam. 2018. “Encoder-Decoder with Atrous Separable Convolution for Semantic Image Segmentation.” In *Computer Vision – ECCV 2018*, 833–51. Lecture Notes in Computer Science. Cham: Springer International Publishing.

Chung, Won-Suk, Christina A. Welsh, Ben A. Barres, and Beth Stevens. 2015. “Do Glia Drive Synaptic and Cognitive Impairment in Disease?” *Nature Neuroscience* 18 (11): 1539–45.

Çiçek, Özgün, Ahmed Abdulkadir, Soeren S. Lienkamp, Thomas Brox, and Olaf Ronneberger. 2016. “3D U-Net: Learning Dense Volumetric Segmentation from Sparse Annotation.” In *Medical Image Computing and Computer-Assisted Intervention – MICCAI 2016*, 424–32. Springer International Publishing.

Creators Jeremy Maitin-Shepard Alex Baden1 William Silversmith2 Eric Perlman3 Forrest Collman4 Tim Blakely5 Jan Funke Chris Jordan Ben Falk6 Nico Kemnitz7 tingzhao Chris Roat Manuel Castro Sridhar Jagannathan8 moenigin Jody Clements Austin Hoag9 Bill Katz10 Dave Parsons Jingpeng Wu11 Lee Kamentsky Pavel Chervakov Philip Hubbard12 Stuart Berg John Hoffer13 Akhilesh Halageri Christian Machacek Kevin Mader Lutz Roeder14 Peter H. Li Show affiliations 1. @omnisci 2. Seung Lab @ Princeton University 3. Yikes LLC 4. Allen Institute for Brain Science 5. @google 6. @stsci 7. @seung-lab @zettaai 8. Charité Universitätsmedizin Berlin 9. Princeton University 10. Janelia Research Center 11. @flatironinstitute 12. Howard Hughes Medical Institute, Janelia Research Campus 13. Harvard 14. @microsoft. n.d. *Google/neuroglancer:* https://doi.org/10.5281/zenodo.5573294.

Crowther, R. A. 1991. “Straight and Paired Helical Filaments in Alzheimer Disease Have a Common Structural Unit.” *Proceedings of the National Academy of Sciences of the United States of America* 88 (6): 2288–92.

Cummings, Jeffrey, Yadi Zhou, Garam Lee, Kate Zhong, Jorge Fonseca, and Feixiong Cheng. 2024. “e12465 10.1002/trc2.12465 New therapies to prevent or delay the onset of symptoms, slow progression, or improve cognitive and behavioral symptoms of Alzheimer’s disease (AD) are needed. We interrogated clinicaltrials.gov including all clinical trials assessing pharmaceutical therapies for AD active in on January 1, 2024. We used the Common Alzheimer's Disease Research Ontology (CADRO) to classify the targets of therapies in the pipeline. There are 164 trials assessing 127 drugs across the 2024 AD pipeline. There were 48 trials in Phase 3 testing 32 drugs, 90 trials in Phase 2 assessing 81 drugs, and 26 trials in Phase 1 testing 25 agents. Of the 164 trials, 34% (N = 56) assess disease-modifying biological agents, 41% (N = 68) test disease-modifying small molecule drugs, 10% (N = 17) evaluate cognitive enhancing agents, and 14% (N = 23) test drugs for the treatment of neuropsychiatric symptoms. Compared to the 2023 pipeline, there are fewer trials (164 vs. 187), fewer drugs (127 vs. 141), fewer new chemical entities (88 vs. 101), and a similar number of repurposed agents (39 vs. 40). In the 2024 Alzheimer's disease drug development pipeline, there are 164 clinical trials assessing 127 drugs.The 2024 Alzheimer's disease drug development pipeline has contracted compared to the 2023 Alzheimer pipeline with fewer trials, fewer drugs, and fewer new chemical entities.Drugs in the Alzheimer's disease drug development pipeline target a wide array of targets; the most common processes targeted include neurotransmitter receptors, inflammation, amyloid, and synaptic plasticity.The total development time for a potential Alzheimer's disease therapy to progress from nonclinical studies to FDA review is approximately 13 years. © 2024 The

Authors. Alzheimer's & Dementia: Translational Research & Clinical Interventions published by Wiley Periodicals LLC on behalf of Alzheimer's Association. Cummings Jeffrey J Chambers-Grundy Center for Transformative Neuroscience Department of Brain Health School of Integrated Health Sciences University of Nevada, Las Vegas (UNLV) Las Vegas Nevada USA. Zhou Yadi Y Genomic Medicine Institute Lerner Research Institute, Cleveland Clinic Cleveland Ohio USA. Lee Garam G Chambers-Grundy Center for Transformative Neuroscience Department of Brain Health School of Integrated Health Sciences University of Nevada, Las Vegas (UNLV) Las Vegas Nevada USA. Zhong Kate K Chambers-Grundy Center for Transformative Neuroscience Department of Brain Health School of Integrated Health Sciences University of Nevada, Las Vegas (UNLV) Las Vegas Nevada USA. Fonseca Jorge J Howard R Hughes College of Engineering Department of Computer Science University of Nevada, Las Vegas (UNLV) Las Vegas Nevada USA. Cheng Feixiong F Genomic Medicine Institute Lerner Research Institute, Cleveland Clinic Cleveland Ohio USA. Department of Molecular Medicine Cleveland Clinic Lerner College of Medicine Case Western Reserve University Cleveland Ohio USA. Case Comprehensive Cancer Center Case Western Reserve University School of Medicine Cleveland Ohio USA. Cleveland Clinic Genome Center Lerner Research Institute, Cleveland Clinic Cleveland Ohio USA. dut R21 AG083003 AG NIA NIH HHS United States R01 AG082118 AG NIA NIH HHS United States P20 AG068053 AG NIA NIH HHS United States R01 AG084250 AG NIA NIH HHS United States RF1 NS133812 NS NINDS NIH HHS United States U01 AG073323 AG NIA NIH HHS United States R01 AG066707 AG NIA NIH HHS United States R01 AG076448 AG NIA NIH HHS United States P20 GM109025 GM NIGMS NIH HHS United States R35 AG071476 AG NIA NIH HHS United States RF1 AG082211 AG NIA NIH HHS United States English Abstract Journal Article Review Alzheimer's disease drug development pipeline: 2024. 2024 04 24." *Alzheimer's & dementia (New York, N. Y.)* 10 (2): e12465.

D'Andrea, Laura, Ramona Stringhi, Monica Di Luca, and Elena Marcello. 2021. "Looking at Alzheimer's Disease Pathogenesis from the Nuclear Side." *Biomolecules* 11 (9): 1261.

Danis, Clément, Elian Dupré, Orgeta Zejneli, Raphaëlle Caillierez, Alexis Arrial, Séverine Bégard, Justine Mortelecque, et al. 2022. "Inhibition of Tau Seeding by Targeting Tau Nucleation Core within Neurons with a Single Domain Antibody Fragment." *Molecular Therapy: The Journal of the American Society of Gene Therapy* 30 (4): 1484–99.

Davies, C. A., D. M. Mann, P. Q. Sumpter, and P. O. Yates. 1987. "A Quantitative Morphometric Analysis of the Neuronal and Synaptic Content of the Frontal and Temporal Cortex in Patients with Alzheimer's Disease." *Journal of the Neurological Sciences* 78 (2): 151–64.

De Genst, Erwin J., Tim Guilliams, Joke Wellens, Elizabeth M. O'Day, Christopher A. Waudby, Sarah Meehan, Mireille Dumoulin, et al. 2010. "Structure and Properties of a Complex of α-Synuclein and a Single-Domain Camelid Antibody." *Journal of Molecular Biology* 402 (2): 326–43.

DeKosky, S. T., and S. W. Scheff. 1990. "Synapse Loss in Frontal Cortex Biopsies in Alzheimer's Disease: Correlation with Cognitive Severity." *Annals of Neurology* 27 (5): 457–64.

Deszyński, Piotr, Jakub Młokosiewicz, Adam Volanakis, Igor Jaszczyszyn, Natalie Castellana, Stefano Bonissone, Rajkumar Ganesan, and Konrad Krawczyk. 2021. "INDI—integrated Nanobody Database for Immunoinformatics." *Nucleic Acids Research* 50 (D1): D1273–81.

Domínguez-Álvaro, M., M. Montero-Crespo, L. Blazquez-Llorca, R. Insausti, J. DeFelipe, and L. Alonso-Nanclares. 2018. "Three-Dimensional Analysis of Synapses in the Transentorhinal Cortex of Alzheimer's Disease Patients." *Acta Neuropathologica Communications* 6 (1). https://doi.org/10.1186/s40478-018-0520-6.

Fang, Michael, Jiaqi Hu, Jordan Weiss, David S. Knopman, Marilyn Albert, B. Gwen Windham,

Keenan A. Walker, et al. 2025. “Lifetime Risk and Projected Burden of Dementia.” *Nature Medicine*, January, 1–5.

Fang, Tao, Xiaotang Lu, Daniel Berger, Christina Gmeiner, Julia Cho, Richard Schalek, Hidde Ploegh, and Jeff Lichtman. 2018. “Nanobody Immunostaining for Correlated Light and Electron Microscopy with Preservation of Ultrastructure.” *Nature Methods* 15 (12): 1029–32.

Ferrer, Ismael, Chadni Sanyal, Marie-Jo Moutin, and Damaris N. Lorenzo. 2024. “Putting the Brakes on Axonal Branching.” *Trends in Neurosciences*, May. https://doi.org/10.1016/j.tins.2024.05.001.

Flury, Anna, Leen Aljayousi, Hye-Jin Park, Mohammadparsa Khakpour, Jack Mechler, Siaresh Aziz, Jackson D. McGrath, et al. 2024. “A Neurodegenerative Cellular Stress Response Linked to Dark Microglia and Toxic Lipid Secretion.” *Neuron* 0 (0). https://doi.org/10.1016/j.neuron.2024.11.018.

Gouras, Gunnar K., Davide Tampellini, Reisuke H. Takahashi, and Estibaliz Capetillo-Zarate. 2010. “Intraneuronal Beta-Amyloid Accumulation and Synapse Pathology in Alzheimer’s Disease.” *Acta Neuropathologica* 119 (5): 523–41.

Gowrishankar, Swetha, Peng Yuan, Yumei Wu, Matthew Schrag, Summer Paradise, Jaime Grutzendler, Pietro De Camilli, and Shawn M. Ferguson. 2015. “Massive Accumulation of Luminal Protease-Deficient Axonal Lysosomes at Alzheimer’s Disease Amyloid Plaques.” *Proceedings of the National Academy of Sciences of the United States of America* 112 (28): E3699–3708.

Habicht, Gernot, Christian Haupt, Ralf P. Friedrich, Peter Hortschansky, Carsten Sachse, Jessica Meinhardt, Karin Wieligmann, et al. 2007. “Directed Selection of a Conformational Antibody Domain That Prevents Mature Amyloid Fibril Formation by Stabilizing Abeta Protofibrils.” *Proceedings of the National Academy of Sciences of the United States of America* 104 (49): 19232–37.

Hampel, Harald, John Hardy, Kaj Blennow, Christopher Chen, George Perry, Seung Hyun Kim, Victor L. Villemagne, et al. 2021. “The Amyloid-β Pathway in Alzheimer’s Disease.” *Molecular Psychiatry* 26 (10): 5481–5503.

Han, Xiaomeng, Xiaotang Lu, Peter H. Li, Shuohong Wang, Richard Schalek, Yaron Meirovitch, Zudi Lin, et al. 2024. “Multiplexed Volumetric CLEM Enabled by scFvs Provides Insights into the Cytology of Cerebellar Cortex.” *Nature Communications* 15 (1): 6648.

Hayworth, K. J., N. Kasthuri, R. Schalek, and J. W. Lichtman. 2006. “Automating the Collection of Ultrathin Serial Sections for Large Volume TEM Reconstructions.” *Microscopy and Microanalysis: The Official Journal of Microscopy Society of America, Microbeam Analysis Society, Microscopical Society of Canada* 12 (S02): 86–87.

He, K., X. Zhang, S. Ren, and J. Sun. n.d. “Deep Residual Learning for Image Recognition.” http://openaccess.thecvf.com/content_cvpr_2016/html/He_Deep_Residual_Learning_CVPR_2016_paper.html.

Hoffman, David P., Gleb Shtengel, C. Shan Xu, Kirby R. Campbell, Melanie Freeman, Lei Wang, Daniel E. Milkie, et al. n.d. “Correlative Three-Dimensional Super-Resolution and Block Face Electron Microscopy of Whole Vitreously Frozen Cells.” https://doi.org/10.1101/773986.

Hooli, B. V., C. M. Lill, K. Mullin, D. Qiao, C. Lange, and L. Bertram. 2015. “PLD3 Gene Variants and Alzheimer’s Disease.” *Nature*. https://www.nature.com/articles/nature14040.

Im, Kyuseok, Sergey Mareninov, M. Fernando Palma Diaz, and William H. Yong. 2019. “An Introduction to Performing Immunofluorescence Staining.” *Methods in Molecular Biology* 1897:299–311.

Januszewski, Michal, and Viren Jain. 2019. “Segmentation-Enhanced CycleGAN.” *bioRxiv*. bioRxiv. https://doi.org/10.1101/548081.

Januszewski, Michał, Jörgen Kornfeld, Peter H. Li, Art Pope, Tim Blakely, Larry Lindsey,

1063 Jeremy Maitin-Shepard, Mike Tyka, Winfried Denk, and Viren Jain. 2018. “High-Precision
1064 Automated Reconstruction of Neurons with Flood-Filling Networks.” *Nature Methods* 15 (8):
1065 605–10.
1066 Jiang, Yi, Linlin Li, Keliang Pang, Jiazheng Liu, Bohao Chen, Jingbin Yuan, Lijun Shen, Xi
1067 Chen, Bai Lu, and Hua Han. 2022. “Synaptic Degeneration in the Prefrontal Cortex of a Rat
1068 AD Model Revealed by Volume Electron Microscopy.” *Journal of Molecular Cell Biology* 14
1069 (3). https://doi.org/10.1093/jmcb/mjac012.
1070 John, Albin, and P. Hemachandra Reddy. 2021. “Synaptic Basis of Alzheimer’s Disease: Focus
1071 on Synaptic Amyloid Beta, P-Tau and Mitochondria.” *Ageing Research Reviews* 65
1072 (101208): 101208.
1073 Johnson, Erik C. B., E. Kathleen Carter, Eric B. Dammer, Duc M. Duong, Ekaterina S.
1074 Gerasimov, Yue Liu, Jiaqi Liu, et al. 2022. “Large-Scale Deep Multi-Layer Analysis of
1075 Alzheimer’s Disease Brain Reveals Strong Proteomic Disease-Related Changes Not
1076 Observed at the RNA Level.” *Nature Neuroscience* 25 (2): 213–25.
1077 Johnson, Erik C. B., Eric B. Dammer, Duc M. Duong, Lingyan Ping, Maotian Zhou, Luming Yin,
1078 Lenora A. Higginbotham, et al. 2020. “Large-Scale Proteomic Analysis of Alzheimer’s
1079 Disease Brain and Cerebrospinal Fluid Reveals Early Changes in Energy Metabolism
1080 Associated with Microglia and Astrocyte Activation.” *Nature Medicine* 26 (5): 769–80.
1081 Karlupia, Neha, Richard L. Schalek, Yuelong Wu, Yaron Meirovitch, Donglai Wei, Alexander W.
1082 Charney, Brian H. Kopell, and Jeff W. Lichtman. 2023. “Immersion Fixation and Staining of
1083 Multi-Cubic Millimeter Volumes for Electron Microscopy-Based Connectomics of Human
1084 Brain Biopsies.” *Biological Psychiatry*, February.
1085 https://doi.org/10.1016/j.biopsych.2023.01.025.
1086 Kasthuri, Narayanan, Kenneth Jeffrey Hayworth, Daniel Raimund Berger, Richard Lee Schalek,
1087 José Angel Conchello, Seymour Knowles-Barley, Dongil Lee, et al. 2015. “Saturated
1088 Reconstruction of a Volume of Neocortex.” *Cell* 162 (3): 648–61.
1089 Kelly, Louise, Mohsen Seifi, Ruolin Ma, Scott J. Mitchell, Uwe Rudolph, Kirsten L. Viola, William
1090 L. Klein, Jeremy J. Lambert, and Jerome D. Swinny. 2021. “Identification of Intraneuronal
1091 Amyloid Beta Oligomers in Locus Coeruleus Neurons of Alzheimer’s Patients and Their
1092 Potential Impact on Inhibitory Neurotransmitter Receptors and Neuronal Excitability.”
1093 *Neuropathology and Applied Neurobiology* 47 (4): 488–505.
1094 Kislinger, Georg, Gunar Fabig, Antonia Wehn, Lucia Rodriguez, Hanyi Jiang, Cornelia Niemann,
1095 Andrey S. Klymchenko, et al. 2023. “ATUM-Tomo: A Multi-Scale Approach to Cellular
1096 Ultrastructure by Combined Volume Scanning Electron Microscopy and Electron
1097 Tomography.” *eLife*. https://doi.org/10.7554/elife.90565.1.
1098 Kislinger, Georg, Cornelia Niemann, Lucia Rodriguez, Hanyi Jiang, Maryam K. Fard, Nicolas
1099 Snaidero, Adrian-Minh Schumacher, Martin Kerschensteiner, Thomas Misgeld, and Martina
1100 Schifferer. 2023. “Neurons on Tape: Automated Tape Collecting Ultramicrotomy-Mediated
1101 Volume EM for Targeting Neuropathology.” Edited by Kedar Narayan, Lucy Collinson, and
1102 Paul Verkade. *Methods in Cell Biology* 177 (February):125–70.
1103 Knott, G., H. Marchman, D. Wall, and B. Lich. 2008. “Serial Section Scanning Electron
1104 Microscopy of Adult Brain Tissue Using Focused Ion Beam Milling.” *Journal of*
1105 *Neuroscience*. https://doi.org/10.1523/jneurosci.3189-07.2008.
1106 Knupp, Allison, Swati Mishra, Refugio Martinez, Jacquelyn E. Braggin, Marcell Szabo, Chizuru
1107 Kinoshita, Dale W. Hailey, Scott A. Small, Suman Jayadev, and Jessica E. Young. 2020.
1108 “Depletion of the AD Risk Gene SORL1 Selectively Impairs Neuronal Endosomal Traffic
1109 Independent of Amyloidogenic APP Processing.” *Cell Reports* 31 (9): 107719.
1110 Koffie, Robert M., Bradley T. Hyman, and Tara L. Spires-Jones. 2011. “Alzheimer’s Disease:
1111 Synapses Gone Cold.” *Molecular Neurodegeneration* 6 (1): 63.
1112 Koffie, Robert M., Melanie Meyer-Luehmann, Tadafumi Hashimoto, Kenneth W. Adams,

Matthew L. Mielke, Monica Garcia-Alloza, Kristina D. Micheva, et al. 2009. “Oligomeric Amyloid β Associates with Postsynaptic Densities and Correlates with Excitatory Synapse Loss near Senile Plaques.” *Proceedings of the National Academy of Sciences* 106 (10): 4012–17.

Kuan, Aaron T., Giulio Bondanelli, Laura N. Driscoll, Julie Han, Minsu Kim, David G. C. Hildebrand, Brett J. Graham, et al. 2024. “Synaptic Wiring Motifs in Posterior Parietal Cortex Support Decision-Making.” *Nature* 627 (8003): 367–73.

Lafaye, Pierre, Ikbel Achour, Patrick England, Charles Duyckaerts, and François Rougeon. 2009. “Single-Domain Antibodies Recognize Selectively Small Oligomeric Forms of Amyloid β, Prevent Aβ-Induced Neurotoxicity and Inhibit Fibril Formation.” *Molecular Immunology* 46 (4): 695–704.

Lafaye, Pierre, Sylvie Bay, Benoît Delatour, Marc Dhenain, Charles Duyckaerts, Tengfei Li, Matthias Vandesquille, Christian Czech, and Fiona Grueninger. 2019. Camelid single-domain antibody directed against amyloid bêta and methods for producing conjugates thereof. EPO 3068799:B1. *European Patent*, filed November 13, 2014, and issued August 28, 2019. https://patentimages.storage.googleapis.com/06/2d/dd/30cf8941c20327/EP3068799B1.pdf.

Lafaye, Pierre, Sylvie Bay, Benoit Delatour, Marc Dhenain, Charles Duyckaerts, Tengfei Li, Matthias Vandesquille, Christian Czech, and Fiona Grueninger. 2020. Camelid single-domain antibody directed against phosphorylated tau proteins and methods for producing conjugates thereof. USPTO 20200165329:A1. *US Patent*, filed December 2, 2019, and issued May 28, 2020. https://patentimages.storage.googleapis.com/88/2f/7a/dd7804c87c4ce3/US20200165329A1.pdf.

LaFerla, Frank M., Kim N. Green, and Salvatore Oddo. 2007. “Intracellular Amyloid-Beta in Alzheimer’s Disease.” *Nature Reviews. Neuroscience* 8 (7): 499–509.

Lee, Wei-Chung Allen, Vincent Bonin, Michael Reed, Brett J. Graham, Greg Hood, Katie Glattfelder, and R. Clay Reid. 2016. “Anatomy and Function of an Excitatory Network in the Visual Cortex.” *Nature* 532 (7599): 370–74.

Lin, Zudi, Donglai Wei, Jeff Lichtman, and Hanspeter Pfister. 2021. “PyTorch Connectomics: A Scalable and Flexible Segmentation Framework for EM Connectomics.” *arXiv [eess.IV]*. arXiv. http://arxiv.org/abs/2112.05754.

Li, Tengfei, Matthias Vandesquille, Fani Koukouli, Clémence Dudeffant, Ihsen Youssef, Pascal Lenormand, Christelle Ganneau, et al. 2016. “Camelid Single-Domain Antibodies: A Versatile Tool for in Vivo Imaging of Extracellular and Intracellular Brain Targets.” *Journal of Controlled Release: Official Journal of the Controlled Release Society* 243 (December):1–10.

Li, Xiaoyu, Yatender Kumar, Hans Zempel, Eva-Maria Mandelkow, Jacek Biernat, and Eckhard Mandelkow. 2011. “Novel Diffusion Barrier for Axonal Retention of Tau in Neurons and Its Failure in Neurodegeneration.” *The EMBO Journal* 30 (23): 4825–37.

Loomba, Sahil, Jakob Straehle, Vijayan Gangadharan, Natalie Heike, Abdelrahman Khalifa, Alessandro Motta, Niansheng Ju, et al. 2022. “Connectomic Comparison of Mouse and Human Cortex.” *Science* 377 (6602): eabo0924.

Magistri, Marco, Dmitry Velmeshev, Madina Makhmutova, and Mohammad Ali Faghihi. 2015. “Transcriptomics Profiling of Alzheimer’s Disease Reveal Neurovascular Defects, Altered Amyloid-β Homeostasis, and Deregulated Expression of Long Noncoding RNAs.” *Journal of Alzheimer’s Disease: JAD* 48 (3): 647–65.

Mandelkow, E. M., and E. Mandelkow. 1998. “Tau in Alzheimer’s Disease.” *Trends in Cell Biology* 8 (11): 425–27.

Martin, Elodie, Mohamed El-Behi, Bertrand Fontaine, and Cecile Delarasse. 2017. “Analysis of

Microglia and Monocyte-Derived Macrophages from the Central Nervous System by Flow Cytometry." *Journal of Visualized Experiments*, no. 124 (June). https://doi.org/10.3791/55781.

Martínez-Carmona, Marina, Fernando Lucas-Ruiz, Alejandro Gallego-Ortega, Caridad Galindo-Romero, María Norte-Muñoz, María José González-Riquelme, Francisco J. Valiente-Soriano, Manuel Vidal-Sanz, and Marta Agudo-Barriuso. 2021. "Ly6c as a New Marker of Mouse Blood Vessels: Qualitative and Quantitative Analyses on Intact and Ischemic Retinas." *International Journal of Molecular Sciences* 23 (1): 19.

Martínez-Serra, Raquel, Lidia Alonso-Nanclares, Kwangwook Cho, and K. Peter Giese. 2022. "Emerging Insights into Synapse Dysregulation in Alzheimer's Disease." *Brain Communications* 4 (2): fcac083.

Mathys, Hansruedi, Jose Davila-Velderrain, Zhuyu Peng, Fan Gao, Shahin Mohammadi, Jennie Z. Young, Madhvi Menon, et al. 2019. "Single-Cell Transcriptomic Analysis of Alzheimer's Disease." *Nature* 570 (7761): 332–37.

McMahon, Conor, Alexander S. Baier, Roberta Pascolutti, Marcin Wegrecki, Sanduo Zheng, Janice X. Ong, Sarah C. Erlandson, et al. 2018. "Yeast Surface Display Platform for Rapid Discovery of Conformationally Selective Nanobodies." *Nature Structural & Molecular Biology* 25 (3): 289–96.

Meftah, Soraya, and Jian Gan. 2023. "Alzheimer's Disease as a Synaptopathy: Evidence for Dysfunction of Synapses during Disease Progression." *Frontiers in Synaptic Neuroscience* 15 (March):1129036.

Meirovitch, Yaron, Lu Mi, Hayk Saribekyan, Alexander Matveev, David Rolnick, and Nir Shavit. 2018. "Cross-Classification Clustering: An Efficient Multi-Object Tracking Technique for 3-D Instance Segmentation in Connectomics." *arXiv [cs.CV]*. arXiv. http://openaccess.thecvf.com/content_CVPR_2019/html/Meirovitch_Cross-Classification_Clustering_An_Efficient_Multi-Object_Tracking_Technique_for_3-D_Instance_CVPR_2019_paper.html.

MICrONS Consortium, J. Alexander Bae, Mahaly Baptiste, Agnes L. Bodor, Derrick Brittain, Joann Buchanan, Daniel J. Bumbarger, et al. 2021. "Functional Connectomics Spanning Multiple Areas of Mouse Visual Cortex." *bioRxiv*. https://doi.org/10.1101/2021.07.28.454025.

Mildner, Alexander, Hauke Schmidt, Mirko Nitsche, Doron Merkler, Uwe-Karsten Hanisch, Matthias Mack, Mathias Heikenwalder, Wolfgang Brück, Josef Priller, and Marco Prinz. 2007. "Microglia in the Adult Brain Arise from Ly-6ChiCCR2+ Monocytes Only under Defined Host Conditions." *Nature Neuroscience* 10 (12): 1544–53.

Miyoshi, Emily, Tina Bilousova, Mikhail Melnik, Danyl Fakhrutdinov, Wayne W. Poon, Harry V. Vinters, Carol A. Miller, et al. 2021. "Exosomal Tau with Seeding Activity Is Released from Alzheimer's Disease Synapses, and Seeding Potential Is Associated with Amyloid Beta." *Laboratory Investigation; a Journal of Technical Methods and Pathology* 101 (12): 1605–17.

Montero-Crespo, Marta, Marta Domínguez-Álvaro, Lidia Alonso-Nanclares, Javier DeFelipe, and Lidia Blazquez-Llorca. 2021. "Three-Dimensional Analysis of Synaptic Organization in the Hippocampal CA1 Field in Alzheimer's Disease." *Brain: A Journal of Neurology* 144 (2): 553–73.

Montero-Crespo, Marta, Marta Dominguez-Alvaro, Patricia Rondon-Carrillo, Lidia Alonso-Nanclares, Javier DeFelipe, and Lidia Blazquez-Llorca. 2020. "Three-Dimensional Synaptic Organization of the Human Hippocampal CA1 Field." *eLife* 9 (July):e57013.

Motta, Alessandro, Manuel Berning, Kevin M. Boergens, Benedikt Staffler, Marcel Beining, Sahil Loomba, Philipp Hennig, Heiko Wissler, and Moritz Helmstaedter. 2019. "Dense Connectomic Reconstruction in Layer 4 of the Somatosensory Cortex." *Science* 366 (6469). https://doi.org/10.1126/science.aay3134.

1213 Muyldermans, Serge. 2021. “A Guide to: Generation and Design of Nanobodies.” *The FEBS*
1214 *Journal* 288 (7): 2084–2102.
1215 Nackenoff, Alex G., Timothy J. Hohman, Sarah M. Neuner, Carolyn S. Akers, Nicole C. Weitzel,
1216 Alena Shostak, Shawn M. Ferguson, et al. 2021. “PLD3 Is a Neuronal Lysosomal
1217 Phospholipase D Associated with β-Amyloid Plaques and Cognitive Function in Alzheimer’s
1218 Disease.” *PLoS Genetics* 17 (4): e1009406.
1219 Neuman, Krystina M., Elizabeth Molina-Campos, Timothy F. Musial, Andrea L. Price, Kwang-Jin
1220 Oh, Malerie L. Wolke, Eric W. Buss, Stephen W. Scheff, Elliott J. Mufson, and Daniel A.
1221 Nicholson. 2015. “Evidence for Alzheimer’s Disease-Linked Synapse Loss and
1222 Compensation in Mouse and Human Hippocampal CA1 Pyramidal Neurons.” *Brain*
1223 *Structure & Function* 220 (6): 3143–65.
1224 Nguyen, Tri M., Logan A. Thomas, Jeff L. Rhoades, Ilaria Ricchi, Xintong Cindy Yuan, Arlo
1225 Sheridan, David G. C. Hildebrand, Jan Funke, Wade G. Regehr, and Wei-Chung Allen Lee.
1226 2022. “Structured Cerebellar Connectivity Supports Resilient Pattern Separation.” *Nature*,
1227 November. https://doi.org/10.1038/s41586-022-05471-w.
1228 Noble, Wendy, Diane P. Hanger, Christopher C. J. Miller, and Simon Lovestone. 2013. “The
1229 Importance of Tau Phosphorylation for Neurodegenerative Diseases.” *Frontiers in*
1230 *Neurology* 4 (July):83.
1231 Oddo, Salvatore, Antonella Caccamo, Jason D. Shepherd, M. Paul Murphy, Todd E. Golde,
1232 Rakez Kayed, Raju Metherate, Mark P. Mattson, Yama Akbari, and Frank M. LaFerla.
1233 2003. “Triple-Transgenic Model of Alzheimer’s Disease with Plaques and Tangles:
1234 Intracellular Abeta and Synaptic Dysfunction.” *Neuron* 39 (3): 409–21.
1235 Pang, Keliang, Richeng Jiang, Wei Zhang, Zhengyi Yang, Lin-Lin Li, Makoto Shimozawa,
1236 Simone Tambaro, et al. 2022. “An App Knock-in Rat Model for Alzheimer’s Disease
1237 Exhibiting Aβ and Tau Pathologies, Neuronal Death and Cognitive Impairments.” *Cell*
1238 *Research* 32 (2): 157–75.
1239 Parag, Toufiq, Daniel Berger, Lee Kamentsky, Benedikt Staffler, Donglai Wei, Moritz
1240 Helmstaedter, Jeff W. Lichtman, and Hanspeter Pfister. 2019. “Detecting Synapse Location
1241 and Connectivity by Signed Proximity Estimation and Pruning with Deep Nets.” In *Lecture*
1242 *Notes in Computer Science*, 354–64. Lecture Notes in Computer Science. Cham: Springer
1243 International Publishing.
1244 Pavarino, Elisa C., Emma Yang, Nagaraju Dhanyasi, Mona D. Wang, Flavie Bidel, Xiaotang Lu,
1245 Fuming Yang, et al. 2023. “mEMbrain: An Interactive Deep Learning MATLAB Tool for
1246 Connectomic Segmentation on Commodity Desktops.” *Frontiers in Neural Circuits* 17
1247 (June):952921.
1248 Peddie, Christopher J., Christel Genoud, Anna Kreshuk, Kimberly Meechan, Kristina D.
1249 Micheva, Kedar Narayan, Constantin Pape, et al. 2022. “Volume Electron Microscopy.”
1250 *Nature Reviews. Methods Primers* 2 (July):51.
1251 Rajendran, Lawrence, and Rosa C. Paolicelli. 2018. “Microglia-Mediated Synapse Loss in
1252 Alzheimer’s Disease.” *The Journal of Neuroscience: The Official Journal of the Society for*
1253 *Neuroscience* 38 (12): 2911–19.
1254 Saman, Sudad, Wonhee Kim, Mario Raya, Yvonne Visnick, Suhad Miro, Sarmad Saman, Bruce
1255 Jackson, et al. 2012. “Exosome-Associated Tau Is Secreted in Tauopathy Models and Is
1256 Selectively Phosphorylated in Cerebrospinal Fluid in Early Alzheimer Disease.” *The Journal*
1257 *of Biological Chemistry* 287 (6): 3842–49.
1258 Scheffer, Louis K., C. Shan Xu, Michal Januszewski, Zhiyuan Lu, Shin-Ya Takemura, Kenneth
1259 J. Hayworth, Gary B. Huang, et al. 2020. “A Connectome and Analysis of the Adult
1260 Drosophila Central Brain.” *eLife* 9 (September). https://doi.org/10.7554/eLife.57443.
1261 Scheff, Stephen W., and Douglas A. Price. 2001. “Alzheimer’s Disease-Related Synapse Loss
1262 in the Cingulate Cortex.” *Journal of Alzheimer’s Disease: JAD* 3 (5): 495–505.

———. 2003. “Synaptic Pathology in Alzheimer’s Disease: A Review of Ultrastructural Studies.” *Neurobiology of Aging* 24 (8): 1029–46.

———. 2006. “Alzheimer’s Disease-Related Alterations in Synaptic Density: Neocortex and Hippocampus.” *Journal of Alzheimer’s Disease: JAD* 9 (3 Suppl): 101–15.

Sedgwick, J. D., S. Schwender, H. Imrich, R. Dörries, G. W. Butcher, and V. ter Meulen. 1991. “Isolation and Direct Characterization of Resident Microglial Cells from the Normal and Inflamed Central Nervous System.” *Proceedings of the National Academy of Sciences of the United States of America* 88 (16): 7438–42.

Seo, Junyoung, Yeonbo Sim, Jeewon Kim, Hyunwoo Kim, In Cho, Hoyeon Nam, Young-Gyu Yoon, and Jae-Byum Chang. 2022. “PICASSO Allows Ultra-Multiplexed Fluorescence Imaging of Spatially Overlapping Proteins without Reference Spectra Measurements.” *Nature Communications* 13 (1): 2475.

Shapson-Coe, Alexander, Michał Januszewski, Daniel R. Berger, Art Pope, Yuelong Wu, Tim Blakely, Richard L. Schalek, et al. 2024. “A Petavoxel Fragment of Human Cerebral Cortex Reconstructed at Nanoscale Resolution.” *Science* 384 (6696): eadk4858.

Sievers, Meike, Alessandro Motta, Martin Schmidt, Yagmur Yener, Sahil Loomba, Kun Song, Johannes Bruett, and Moritz Helmstaedter. 2024. “Connectomic Reconstruction of a Cortical Column.” *bioRxiv*. https://doi.org/10.1101/2024.03.22.586254.

Sobotzik, Jürgen-Markus, Jana Maria Sie, Chrisoula Politi, Domenico Del Turco, Vann Bennett, Thomas Deller, and Christian Schultz. 2009. “AnkyrinG Is Required to Maintain Axo-Dendritic Polarity in Vivo.” *Proceedings of the National Academy of Sciences of the United States of America* 106 (41): 17564–69.

St-Pierre, Marie-Kim, Micaël Carrier, Fernando González Ibáñez, Eva Šimončičová, Marie-Josée Wallman, Luc Vallières, Martin Parent, and Marie-Ève Tremblay. 2022. “Ultrastructural Characterization of Dark Microglia during Aging in a Mouse Model of Alzheimer’s Disease Pathology and in Human Post-Mortem Brain Samples.” *Journal of Neuroinflammation* 19 (1): 235.

Swanson, Larry W., and Jeff W. Lichtman. 2016. “From Cajal to Connectome and Beyond.” *Annual Review of Neuroscience* 39 (July):197–216.

Taylor, J. Paul, John Hardy, and Kenneth H. Fischbeck. 2002. “Toxic Proteins in Neurodegenerative Disease.” *Science* 296 (5575): 1991–95.

Tuijtel, Maarten W., A. Koster, S. Jakobs, F. Faas, and T. Sharp. 2019. “Correlative Cryo Super-Resolution Light and Electron Microscopy on Mammalian Cells Using Fluorescent Proteins.” *Scientific Reports* 9 (February). https://doi.org/10.1038/s41598-018-37728-8.

Turner, Nicholas L., Thomas Macrina, J. Alexander Bae, Runzhe Yang, Alyssa M. Wilson, Casey Schneider-Mizell, Kisuk Lee, et al. 2022. “Reconstruction of Neocortex: Organelles, Compartments, Cells, Circuits, and Activity.” *Cell* 185 (6): 1082–1100.e24.

Twohig, Daniel, and Henrietta M. Nielsen. 2019. “α-Synuclein in the Pathophysiology of Alzheimer’s Disease.” *Molecular Neurodegeneration* 14 (1): 23.

Tzioras, Makis, Robert I. McGeachan, Claire S. Durrant, and Tara L. Spires-Jones. 2023. “Synaptic Degeneration in Alzheimer Disease.” *Nature Reviews. Neurology* 19 (1): 19–38.

Urbanc, B., L. Cruz, R. Le, J. Sanders, K. Hsiao Ashe, K. Duff, H. E. Stanley, M. C. Irizarry, and B. T. Hyman. 2002. “Neurotoxic Effects of Thioflavin S-Positive Amyloid Deposits in Transgenic Mice and Alzheimer’s Disease.” *Proceedings of the National Academy of Sciences of the United States of America* 99 (22): 13990–95.

Urbanski, Alysson H., Department of Clinical and Toxicological Analyses, School of Pharmaceutical Sciences, University of Sao Paulo, Sao Paulo, Brazil, José D. Araujo, Rachel Creighton, Helder I. Nakaya, Department of Clinical and Toxicological Analyses, School of Pharmaceutical Sciences, University of Sao Paulo, Sao Paulo, Brazil, Department of Bioengineering, University of Washington, Seattle, WA, USA, Department of

Clinical and Toxicological Analyses, School of Pharmaceutical Sciences, University of Sao Paulo, Sao Paulo, Brazil, and Scientific Platform Pasteur/USP, University of Sao Paulo, Sao Paulo, Brazil. 2019. “Integrative Biology Approaches Applied to Human Diseases.” In *Computational Biology*, 19–36. Codon Publications.

Vilalta, Anna, and Guy C. Brown. 2018. “Neurophagy, the Phagocytosis of Live Neurons and Synapses by Glia, Contributes to Brain Development and Disease.” *The FEBS Journal* 285 (19): 3566–75.

Wei, Lu, Zhixing Chen, Lixue Shi, Rong Long, Andrew V. Anzalone, Luyuan Zhang, Fanghao Hu, Rafael Yuste, Virginia W. Cornish, and Wei Min. 2017. “Super-Multiplex Vibrational Imaging.” *Nature* 544 (7651): 465–70.

“Welcome to NeuroMab!” n.d. Accessed April 13, 2024. https://neuromab.ucdavis.edu/neuromabs.cfm.

Wilson, Andrea C., Brittany N. Dugger, Dennis W. Dickson, and Deng-Shun Wang. 2011. “TDP-43 in Aging and Alzheimer’s Disease - a Review.” *International Journal of Clinical and Experimental Pathology* 4 (2): 147–55.

Wilton, Emily E., Michael P. Opyr, Senthilkumar Kailasam, Ronja F. Kothe, and Hans-Joachim Wieden. 2018. “sdAb-DB: The Single Domain Antibody Database.” *ACS Synthetic Biology* 7 (11): 2480–84.

Wood, Levi B., Ashley R. Winslow, and Samantha Dale Strasser. 2015. “Systems Biology of Neurodegenerative Diseases.” *Integrative Biology: Quantitative Biosciences from Nano to Macro* 7 (7): 758–75.

Yin, Rui-Hua, Jin-Tai Yu, and Lan Tan. 2015. “The Role of SORL1 in Alzheimer’s Disease.” *Molecular Neurobiology* 51 (3): 909–18.

Yu, Meichen, Olaf Sporns, and Andrew J. Saykin. 2021. “The Human Connectome in Alzheimer Disease - Relationship to Biomarkers and Genetics.” *Nature Reviews. Neurology* 17 (9): 545–63.

Zempel, Hans, Frank J. A. Dennissen, Yatender Kumar, Julia Luedtke, Jacek Biernat, Eva-Maria Mandelkow, and Eckhard Mandelkow. 2017. “Axodendritic Sorting and Pathological Missorting of Tau Are Isoform-Specific and Determined by Axon Initial Segment Architecture.” *The Journal of Biological Chemistry* 292 (29): 12192–207.

Zimmermann, Iwan, Pascal Egloff, Cedric A. J. Hutter, Benedikt T. Kuhn, Philipp Bräuer, Simon Newstead, Roger J. P. Dawson, Eric R. Geertsma, and Markus A. Seeger. 2020. “Generation of Synthetic Nanobodies against Delicate Proteins.” *Nature Protocols* 15 (5): 1707–41.

Zuiderveld, K. 1994. “Contrast Limited Adaptive Histogram Equalization.” *Graphics Gems* 0:474–85.